

# **Cellular Solids Project**

## **Image study of the failure mechanisms in dry trabecular whale bone during fracture toughness tests**

*Bruno Gonçalves da Silva*

### **Abstract**

The study of the fracturing of trabecular bone is of particular interest to improve the current knowledge of bone failure that may occur due to osteoporosis and metastatic or benign skeletal tumors, or even due to accidental overloading of a bone. While much effort has been put in experimentally measuring elastic and yield properties of trabecular bone, the fracture toughness and fracturing processes of trabecular bone subject to Mode I loading needs to be better understood.

In this project, dry whale trabecular bone is used to study the fracturing mechanisms that occur when specimens are loaded in three-point bending with an initial mid-span notch. These analyses include the use of a High-Resolution (HR) and a High-Speed Video (HSV) cameras in order to capture the development of cracks and to identify the mechanisms responsible for their propagation. The apparent and solid densities of the specimens were also measured and related to the fracture toughnesses obtained from the three-point bending tests.

From the three-point bending tests performed, it was found that (1) some trabeculae develop in a radial fashion (radial trabeculae), from a focal point approximately at the center of the whale vertebra, (2) there is a strong correlation between the maximum vertical load reached and the slope of the load-displacement curve in the linear elastic regime, (3) the fractures initiate at the notch tip and usually propagate without branching and by stages, causing a load drop every time they propagate, (4) the fracture toughnesses are higher in the specimens cut in the same plane as the radial trabeculae than those parallel to the axis of the vertebra (5) the fracture toughness appears to increase from the outside of the vertebra to the focal point of the radial trabeculae.

## Contents

1	Introduction.....	3
2	Methodology .....	6
2.1	Specimen Preparation .....	6
2.2	Geometry of the specimens.....	6
2.3	Relative Density Measurement.....	8
2.4	Test setup .....	9
3	Test results .....	11
3.1	Specimens with $a = 0.25$ inches ( $\approx 0.64$ cm) .....	11
3.2	Specimens with $a = 0.50$ inches ( $\approx 1.27$ cm) .....	13
3.3	Maximum load vs slope of the load-deflection curves in the linear elastic regime .....	15
3.4	High-Resolution Camera observations .....	15
3.5	High-Speed Video camera observations .....	17
4	Relative density and fracture toughness of the specimens.....	18
5	Summary and Conclusions.....	20
6	References.....	21
7	Appendices.....	23
7.1	Specimens and Cracks Dimensions .....	23
7.2	Relative Density and Fracture Toughness Calculations.....	24
7.3	Image Analyses.....	26

## 1 Introduction

Investigating the mechanical properties of bone is important to better understand how its cortex and trabecular portions deform and fail. Specifically, the study of the fracturing behavior of trabecular bone is of particular interest to improve the current knowledge of bone failure due to osteoporosis and metastatic or benign skeletal tumors, or even due to accidental overloading.

Several authors have been measuring the mechanical properties of trabecular bone experimentally: Bayraktar et al. (2004) and Keavenly et al. (1994 and 1999), for instance, used uniaxial compressive and tensile tests to determine the yield strength and Elastic Modulus of trabecular bone, while Cook and Ziopoulos (2009) used compact and three-point bending tests to determine fracture toughness of human trabecular bone. Others have also collected imaging data in their experiments in order to improve their understanding of the deformation and failure mechanisms in bone: Hardisty et al. (2013) and Thurner et al. (2009) used High-Speed Video cameras to image tension tests in cortical bone of race horses and uniaxial compressive tests in human trabecular bone, respectively. The latter also used the Scanning Electron Microscope (SEM) to evaluate why whitening of the trabecular bone occurs when it is significantly loaded. Micro-photographs were also used by Fyhrie and Schaffler (1994) to assess the various failure mechanisms of trabecular bone when tested under uniaxial compression, while micro-CT imagery was used by Nagaraja et al. (2005) and Muller et al. (1998) during micro-compression tests in order to observe damage initiation, propagation and accumulation.

Despite the number and thoroughness of experiments performed in trabecular bone, not many researchers have experimentally measured Mode I fracture toughness of trabecular bone while simultaneously studying the mechanisms involved in crack propagation using imaging data. In this project, dry whale trabecular bone is used to study the fracturing mechanisms that occur when specimens are loaded in three-point bending with an initial mid-span notch. These analyses include the use of a High-Resolution (HR) and a High-Speed Video (HSV) cameras in order to capture the development of cracks and to identify the mechanisms responsible for their propagation.

The vertebra investigated is one of the first caudal vertebrae of a Humpback whale (as highlighted in Figure 1 which shows the skeleton of a Sperm whale, very similar to the skeleton of a Humpback whale, particularly the vertebral column) that was gently provided by the Massachusetts Division of Fisheries and Wildlife (*MassWildlife*) to Professor Lorna Gibson. The body of the whale washed out in Deer's Island, Massachusetts, and its skeleton was preserved by MassWildlife. The trabecular portion of the whale vertebrae used in this project has a pentagonal shape with the sides measuring from 5" to 6.5" (12.5 cm to 16 cm), approximately, as shown in Figure 2. The whale vertebra was chosen due to the very

uniform and large trabecular portion of the bone, which makes specimen preparation simpler and test results more consistent between different specimens.

The main goals of this study are:

- Measure Mode I fracture toughness of dry trabecular whale bone subject to three-point bending tests;
- Analyze the fracturing processes which occur in dry trabecular whale bone subject to three-point bending tests using High-Speed Video (to observe the quick propagation of cracks near a load peak) and High-Resolution images (to observe the changes in the trabecular bone throughout the test).
- Relate Mode I fracture toughness with the relative density of the trabecular bone studied;
- Evaluate the spatial variation of relative density of dry trabecular bone of a whale vertebra.

This report is organized as follows: Section 2 describes the methodology used in the project, including how the specimens were prepared and how their relative densities were measured, as well as the setup used to perform the three-point bending tests. Section 3 shows the results obtained in the three-point bending tests, not only the load-displacement behavior but also its correlation with the imaging data collected during the test. Section 4 relates the relative density with the fracture toughness of the different specimens tested, and analyzes the spatial variation of the relative density of the trabecular bone studied. Section 5 provides a summary and conclusions reached in the project. At the end of this report, an Appendix section provides the detailed measurements and calculation of the relative density and fracture toughness of the specimens, as well as the most relevant imaging data obtained in the tests

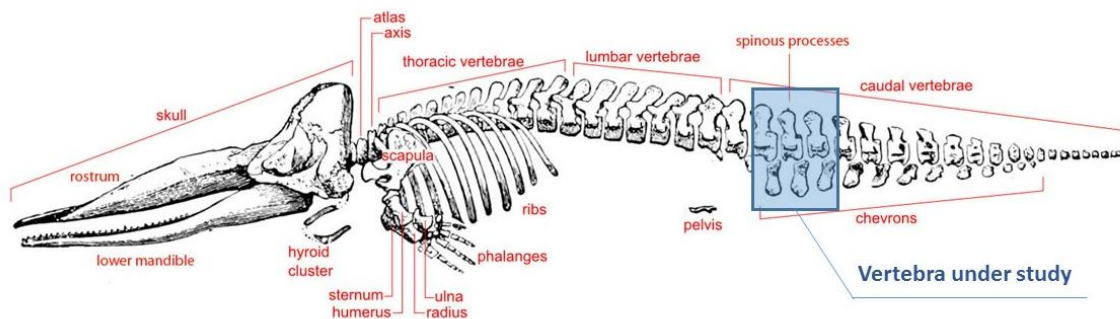


Figure 1 – Sperm whale skeleton showing vertebra under study, one of the first caudal vertebrae (adapted from Aboe, G, [www.onceinawhale.com](http://www.onceinawhale.com), 2013)

Courtesy of Kurzon on [Wikimedia Commons](https://commons.wikimedia.org). License CC BY-SA. This content is excluded from our Creative Commons license. For more information, see <http://ocw.mit.edu/help/faq-fair-use/>.



a)



b)

Figure 2 – a) Top and b) side view of the vertebra of the Humpback whale showing uniform trabecular bone

## 2 Methodology

The whale bone was cut into small beams whose dimensions and relative density were subsequently measured. These beams were then tested in three-point bending. The methodologies used in these different stages are described in the following subsections.

### 2.1 Specimen Preparation

The whale bone was first cut with an OMAX waterjet into a cube with approximately 4.5" ( $\approx 12$  cm) of side length, as shown in Figure 3a. Second, in order to avoid the tapering caused by cutting relatively thick specimens with the waterjet, a wet-saw was used to cut the cube in half, as shown in Figure 3b, and subsequently in smaller beams.

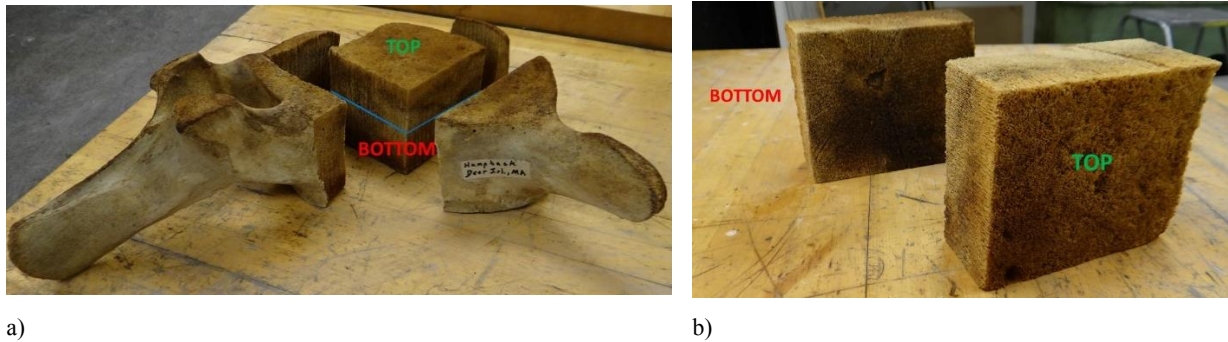


Figure 3 – a) Cube cut with the waterjet and b) top and bottom halves of the cube after being cut with a wet-saw.

### 2.2 Geometry of the specimens

The twelve beams cut with the wet-saw are approximately 4.0" (11 cm)-long, 1.0" (2.5cm)-wide and 0.5" (1.2 cm)-thick, following the ratios proposed by ASTM E-1820 which are shown in Figure 4. Two different cutting orientations were used, as illustrated in Figure 5: four of the beams were cut with their width (W) perpendicular to the axis of the vertebra – Orientation 1, also called in this report direction in the same plane as the radial trabecula – and eight beams were cut with their thickness (B) perpendicular to the axis of the vertebra – Orientation 2, also called direction parallel to the axis of the vertebra. Two different lengths of the initial crack were considered, namely 0.5" (1.27 cm) and 0.25" (0.64 cm). These cracks were created using a mechanical circular saw to open the first 4/5 of the crack length, and subsequently a razor blade to manually open the remaining 1/5 of the crack.

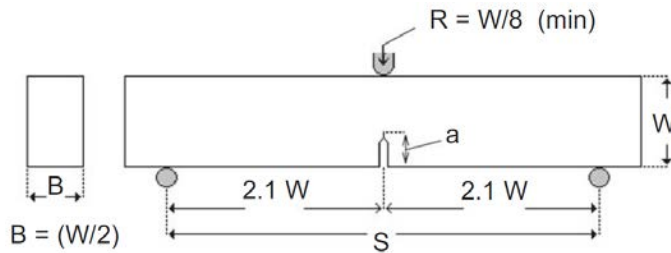


Figure 4 – Geometry of the specimens to be used in the 3-point bending tests (in Cook and Ziopoulos, 2009)  
Courtesy of Elsevier, Inc., <http://www.sciencedirect.com>. Used with permission.

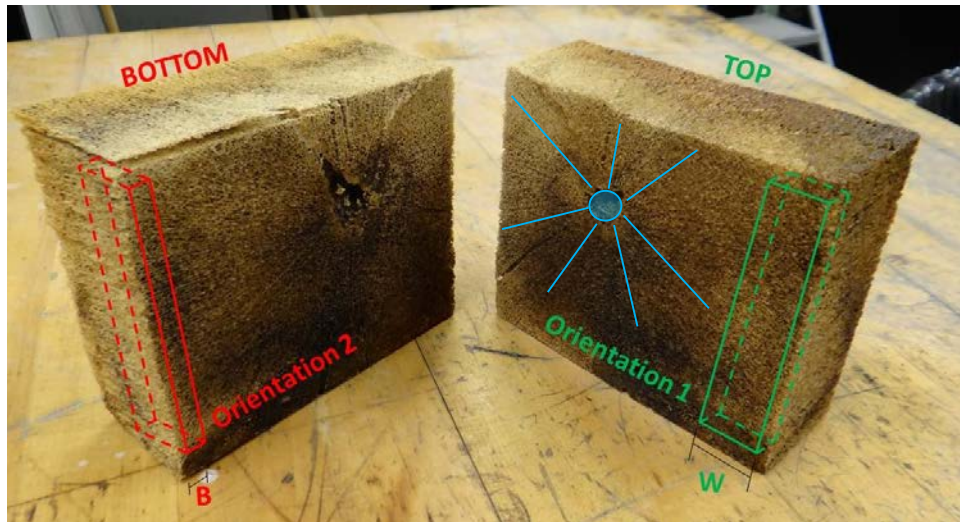


Figure 5 – Cutting orientations of the specimens used in the tests, with blue lines and blue circle showing the radial direction of the trabeculae and focal point of the radial trabeculae, respectively

Table 1 identifies the different cutting orientations and lengths of the initial cracks (a) of the twelve specimens tested. As can be observed in the same table, two different imaging techniques were used in the tests, namely High-Speed video and High-Resolution camera; this will be described in detail in Subsection 2.4 – Test Setup.

Table 1 – Cutting orientations, initial crack lengths and image monitoring used in the specimens tested in three-point bending

Specimen	S (in)	W(in)	B(in)	Orientation of specimen	a (in)	High-Speed Video	High-Resolution Camera
1					0.5	Used	
2							Used
3					0.25	Used	
4							Used
5					0.5	Used	
6							
7							Used
8							
9					0.25	Used	
10							
11							Used
12							Used but images not available

## 2.3 Relative Density Measurement

The relative densities of the specimens were calculated based on the expression:

$$RD = \frac{\rho^*}{\rho_s}$$

Where  $\rho^*$  is the apparent density and  $\rho_s$  is the density of the solid part of the specimen. The apparent density was determined by measuring the weight and the volume of the specimens, as presented in Appendix 7.1 – Specimens and cracks dimensions. The density of the solid part was measured based on a modified version of the ASTM 854 – 14, which is commonly used to determine the specific gravity of soil solids. Based on this ASTM standard, the density in kg/m<sup>3</sup> of the solid fraction of the specimen is given by:

$$\rho_s = \frac{\rho_w \cdot W_s}{W_s + W_{pw} - W_{ps}}$$

Where

- $\rho_w$  is the density of the water, which depends on the temperature of the water used in each specimen (kg/m<sup>3</sup>);
- $W_s$  is the weight of the specimen, measured in a scale (kg);
- $W_{pw}$  is the weight of the pycnometer full of water only (kg);
- $W_{ps}$  is the weight of the pycnometer with water and specimen inside (kg).

In order to obtain precise values of  $\rho_s$ , the following procedure was used to measure  $W_{pw}$  and  $W_{ps}$  ( $W_s$  is simply the weight of the specimen):

- 1- Water is poured into a glass flask (called pycnometer for the purpose of this experiment) to approximately 4/5 of its volume;
- 2- The pycnometer is put inside a pressurizing vessel, as shown in Figure 6a, where a vacuum pressure of approximately 0.4 psi (the atmospheric pressure is 1.0 bar or 14.7 psi) is applied in order to remove air bubbles of the water;
- 3- The pycnometer is then overfilled with water taking advantage of the convex surface that the water produces when a container is slightly overfilled, and subsequently carefully covered with a flat piece of glass (Figure 6b), making sure no air bubbles result of this process. The water that spills when the pycnometer is covered is cleaned with paper tissue and  $W_{pw}$  is then measured;
- 4- Some of the water inside of the pycnometer (approximately 1/4 of the volume) is thrown away and the specimen is put inside of the pycnometer, making sure that it is completely immersed;

- 5- The pycnometer is then taken to the pressurizing vessel, as in step 2, in order to remove all the air bubbles from the specimen;
- 6- After measuring the temperature of the water, the pycnometer is then overfilled with water and covered with a piece of glass, similar to step 3, and  $W_{PS}$  is measured. This is shown in Figure 6c.

Using a flat piece of glass to cover the pycnometer and making sure that there are no air bubbles produced when covering it is important in order to make sure that the volume of the systems used to measure  $W_{PW}$  and  $W_{PS}$  are exactly the same.

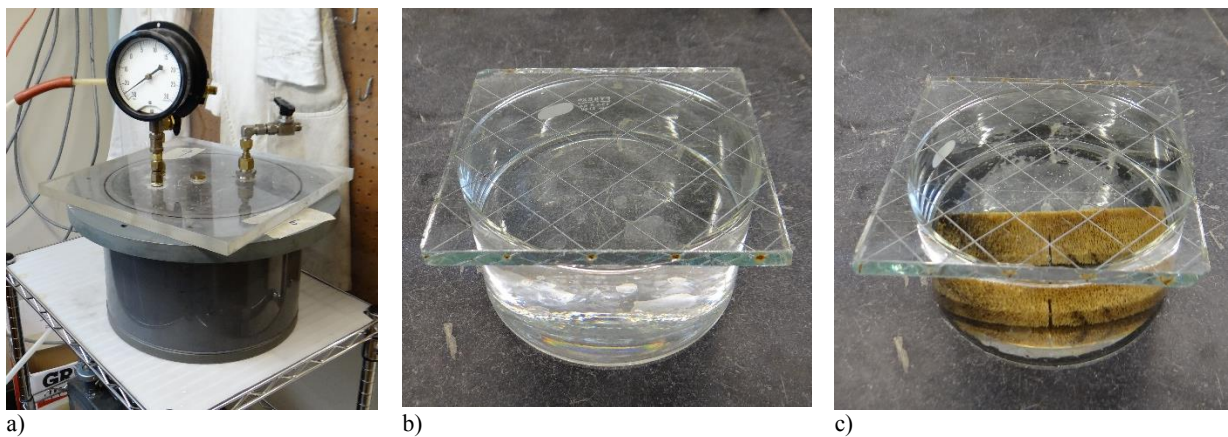
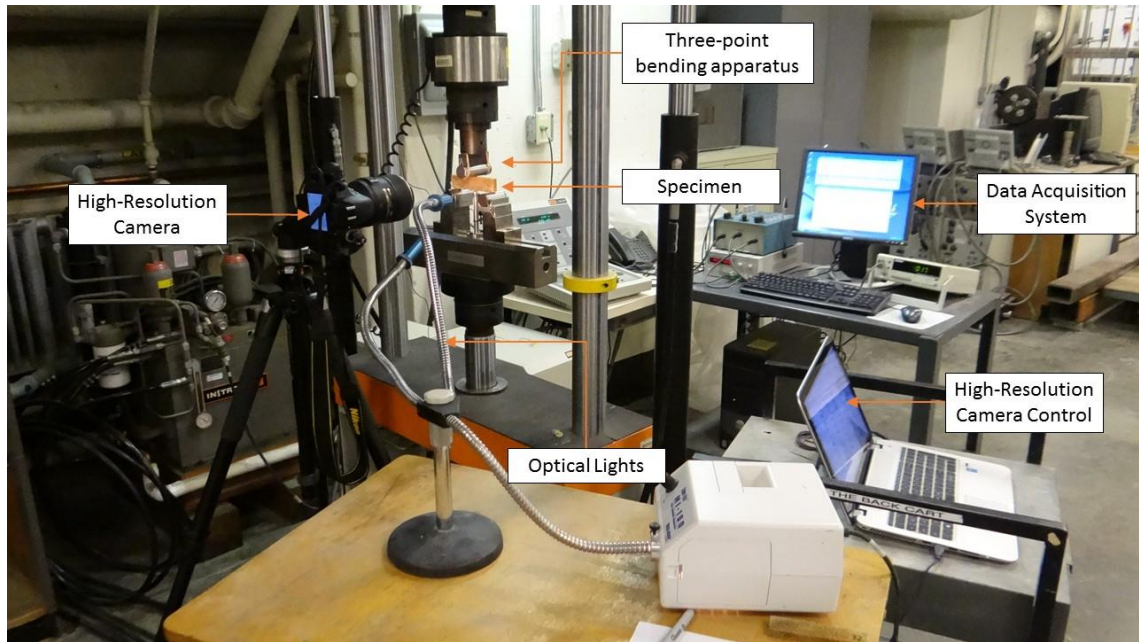


Figure 6 – a) Pressurizing vessel used to de-air the b) water and c) specimen+water inside the pycnometer which is covered by a flat piece of glass to assure that the volume of the system is always the same

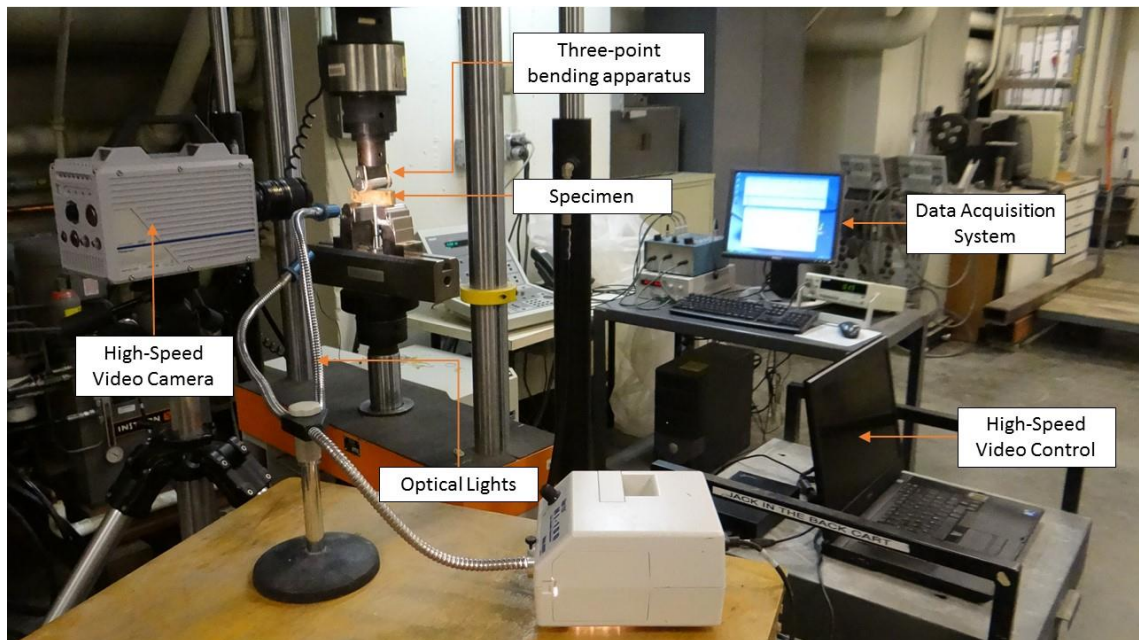
## 2.4 Test setup

The test setup consists of an Instron loading machine where a three-point bending apparatus was mounted, a data acquisition system that logged the vertical load applied to the specimen and the displacement of the cross-head of the loading frame at a sampling rate of 4Hz, and image monitoring devices with their respective computer controls. In order to obtain clear images of the specimens, two optical lights were used to illuminate the specimens. The different components of the test setups are shown in Figures 7a and 7b.

The image monitoring was done with a High-Speed video (HSV) camera and with a High-Resolution (HR) camera. The HSV camera was set to capture three seconds before a manual trigger at 5,000 frames per second at a resolution of 1024 pixel x 1024 pixel, and also allowed the capturing of individual pictures throughout the test with the same resolution. The HSV camera was triggered by the operator, when the propagation of a first crack was observed. The HR camera was used to automatically take pictures with 24 Mpixel of resolution every two seconds throughout the entire test. Only one image monitoring device was used in each test, as shown in Table 1.



a)



b)

Figure 7 – Test setup using a) High-Resolution camera and b) High-Speed Video camera

### 3 Test results

This section describes and analyzes the load-deflection curves and imaging data obtained in the three-point bending tests performed. Subsections 3.1 and 3.2 discuss the load-displacement curves obtained in the tests performed in the specimens with 0.25" and 0.50", respectively. Within each of these subsections, the results obtained with the two cutting orientations will be analyzed. Subsection 3.3 will discuss the relationship between the maximum vertical load ( $P_{\max}$ ) and the slope of the load-displacement curves in the linear elastic regime, and Subsections 3.4 and 3.5 discuss the imaging data obtained with the HR and HSV cameras, respectively.

#### 3.1 Specimens with $a = 0.25$ inches ( $\approx 0.64$ cm)

By analyzing the load vs mid-span deflection curves shown in Figures 8a and 8b, for specimens with Orientation 1 and 2, respectively, one can learn that:

- The maximum load reached by the two specimens with Orientation 1 was 80 N for both specimens, and the slope of the curves in the linear elastic regime (before any crack develops since it causes a change in the slope) is approximately 145 N/mm. This slope could be converted into a modulus of elasticity in bending  $E_f$ , which for three-point bending tests without initial crack is given by:

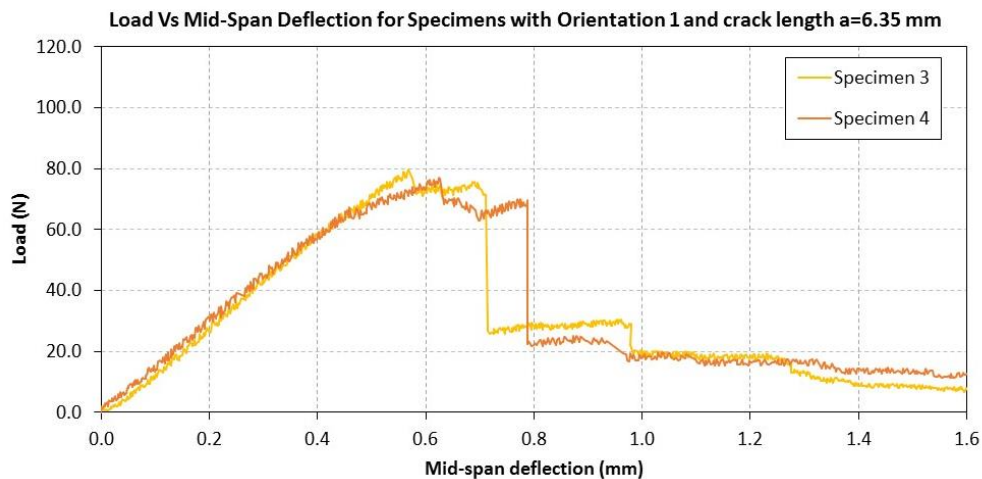
$$E_f = \frac{S^3 m}{4BW^3}$$

using the letters shown in Figure 4 to describe the different dimensions, and with  $m$  being the slope of the load-displacement in the linear elastic regime. However, since a notch has to be created at the mid-span of the beam to perform fracture toughness tests, the  $W$  to be used in the calculations becomes questionable; therefore, only the slope of the load-displacement curve in the linear elastic regime,  $m$ , will be used in these analyses.

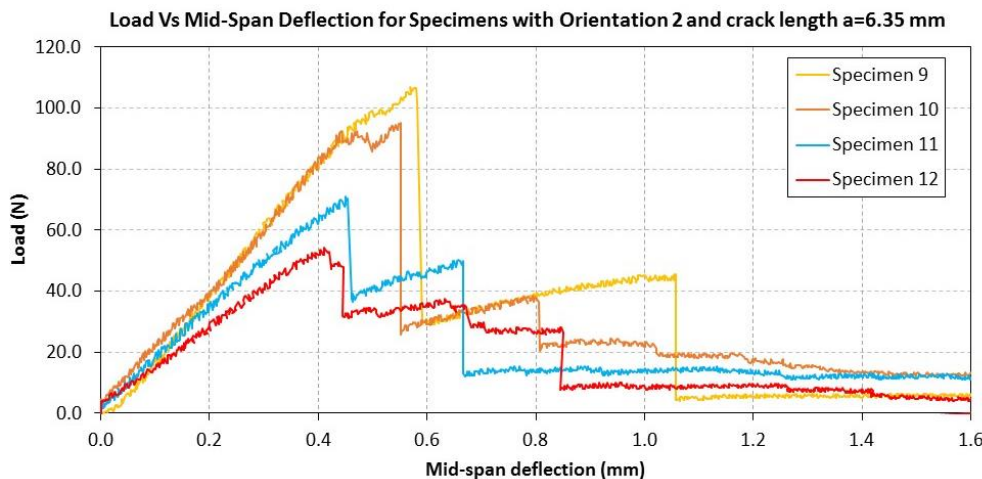
- The maximum load reached by the four specimens with Orientation 2 ranged between 50 N and 105 N and the slope of the curves in the linear elastic regime is approximately 205 N/mm for the two specimens with the highest maximum load and decreases to approximately 150 N/mm and 125 N/mm for the two specimens that reached the lowest maximum loads (Specimens 11 and 12);
- There are usually two significant load drops during the tests for both orientations tested. For the specimens with Orientation 1 these drops occur at a deflection of 0.7mm to 0.8mm and at 0.9mm to 1.0mm. For the specimens with Orientation 2 these two drops occur at a deflection of 0.4mm to 0.6mm and 0.7mm to 1.1mm, showing more variation than in the specimens with Orientation 1. It

also appears that the second drops observed in the specimens with Orientation 2 are more significant than those observed in the specimens with Orientation 1.

The load drops correspond to fractures propagating from the tip of the notch, as will be discussed in greater detail in the Subsections 3.4 and 3.5, in which the imaging results will be shown. However, these fractures do not propagate at once until the specimen fails; they are actually arrested after the first load drop and, in some tests, the specimen can be further loaded, as observed in Specimens 9, 10, 11 and 12. As the test continues, the specimens continue to deform and the stress concentration at the tips of the already developed cracks continue to increase until the crack further propagates. Therefore, the crack propagates in stages, causing a load drop every time it propagates.



a)



b)

Figure 8 – Load versus mid-span deflection for the specimens with initial notch length of 0.25" for a) cutting orientation 1 and b) cutting orientation 2

### **3.2 Specimens with $a = 0.50$ inches ( $\approx 1.27$ cm)**

By analyzing the load vs mid-span deflection curves shown in Figures 9a and 9b, for specimens with Orientation 1 and 2, respectively, one can observe that:

- The maximum load reached by the two specimens with Orientation 1 ranged from 50 N to 70 N, and the slope of the curves in the elastic regime ranged between 75 N/mm and 120 N/mm.
- The maximum load reached by the four specimens with Orientation 2 ranged between 30 N and 50 N and the slope of the curves in the elastic regime ranged from 50 N/mm to 120 N/mm;
- There is one significant load drop during the tests performed in the specimens with Orientation 1, which occurred at a deflection slightly above 0.8mm.
- The number of significant load drops in the specimens with Orientation 2 was variable, ranging from one in Specimen 6 to three in Specimen 8.

By comparing the results obtained with the two initial crack lengths, the maximum loads are, as expected, always greater when  $a=0.25$ " than when  $a=0.50$ " for the same cutting orientations. The mid-span deflection at which the first load-drop is very similar for all the specimens with Orientation 1 regardless the length of the initial crack, occurring at approximately 0.80mm. For Orientation 2, this first drop varied substantially, ranging from 0.40mm to 0.60mm for Orientation 1 and from 0.60mm to 0.80mm for Orientation 2. Furthermore, there appears to be a relationship between the maximum load reached by the specimens ( $P_{max}$ ) and the slope of the load-displacement curve in the linear elastic regime; this relationship will be discussed in the following Subsection 3.3.

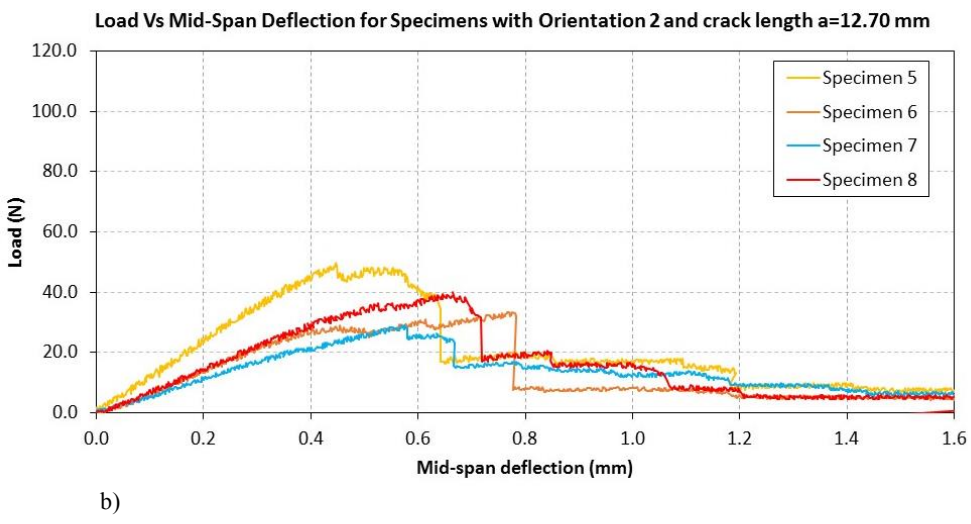
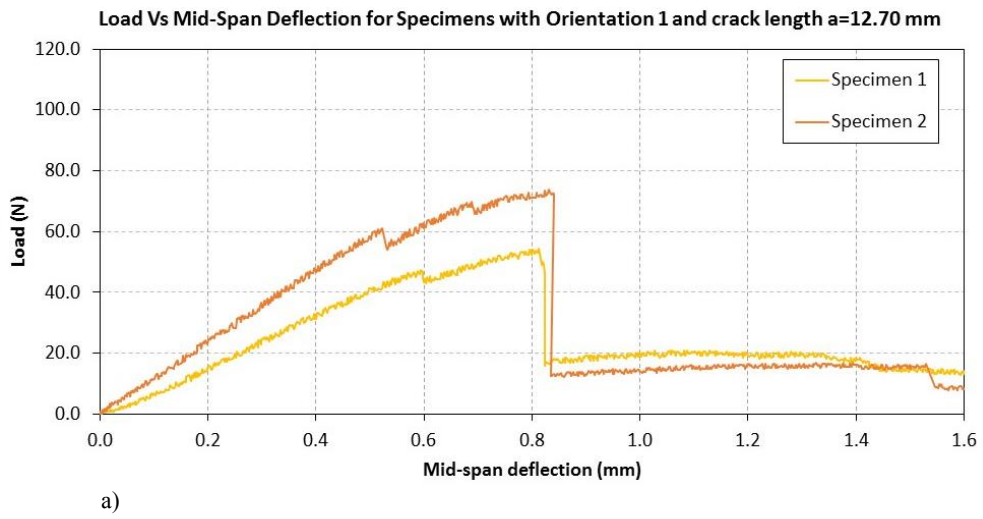


Figure 9 – Load versus mid-span deflection for the specimens with initial notch length of 0.50" for a) cutting orientation 1 and b) cutting orientation 2

### 3.3 Maximum load vs slope of the load-deflection curves in the linear elastic regime

As mentioned earlier, there appears to be a relationship between the maximum vertical load reached in the tests and the slope of the load-displacement curve in the linear elastic regime, as shown in Figure 10 for the 12 specimens tested. The plot confirms that there is a strong relationship, since the data shows a high (0.89) coefficient of determination  $R^2$  obtained for a linear regression. Furthermore, this strong relationship is obtained using all specimens tested, regardless the length of the notch or cutting orientation.

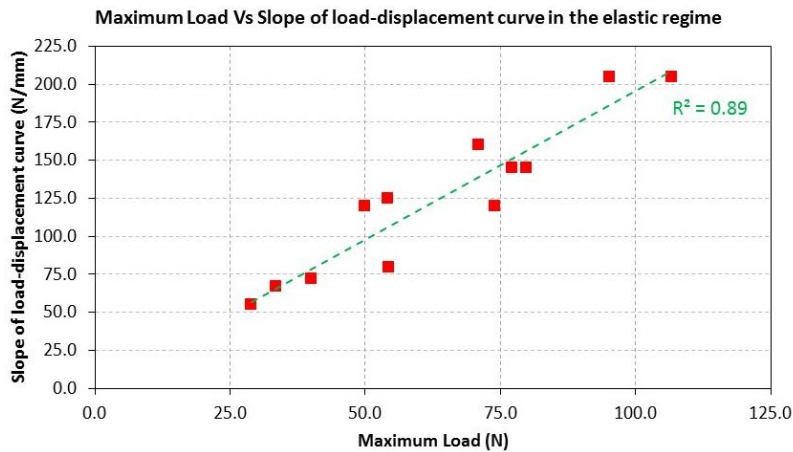


Figure 10 – Maximum load vs inclination of the load-displacement curve in the elastic regime

### 3.4 High-Resolution Camera observations

This subsection analyzes HR pictures obtained in the test performed in Specimen 4. Appendix 7.3 – Image Analysis – presents more imaging data and analysis of the other tests.

In the imaging analysis of Specimen 4, four frames were used, as shown in Figure 11a. Frame 0 was taken at the beginning of the test and Frame 1 was taken slightly before the first crack was visible. The change in slope that can be observed at approximately 0.40mm of mid-span deflection must have occurred due to cracks that are not visible in these HR pictures. Frame 2 was taken after a first small load drop and just before the largest load drop of the test, while Frame 3 was taken just after the same load drop.

By analyzing Figure 11b, one can observe that (1) as it propagates, the crack follows the direction of the radial trabeculae and (2) the crack starts at the notch tip and propagates by increments, causing the load to drop. In Figures 11c and 11d, one can observe in more detail some of the mechanisms involved in the propagation of the crack in this trabecular bone: the crack intersects trabeculae which are usually perpendicular to its direction of propagation, and the intersected trabeculae appear to break in tension and only at a single location in each trabecula. Usually, the cracks propagate without branching, as can be seen in Appendix 7.3; however, Frame 3 in Figure 11b shows a short branch at the top end of the crack.

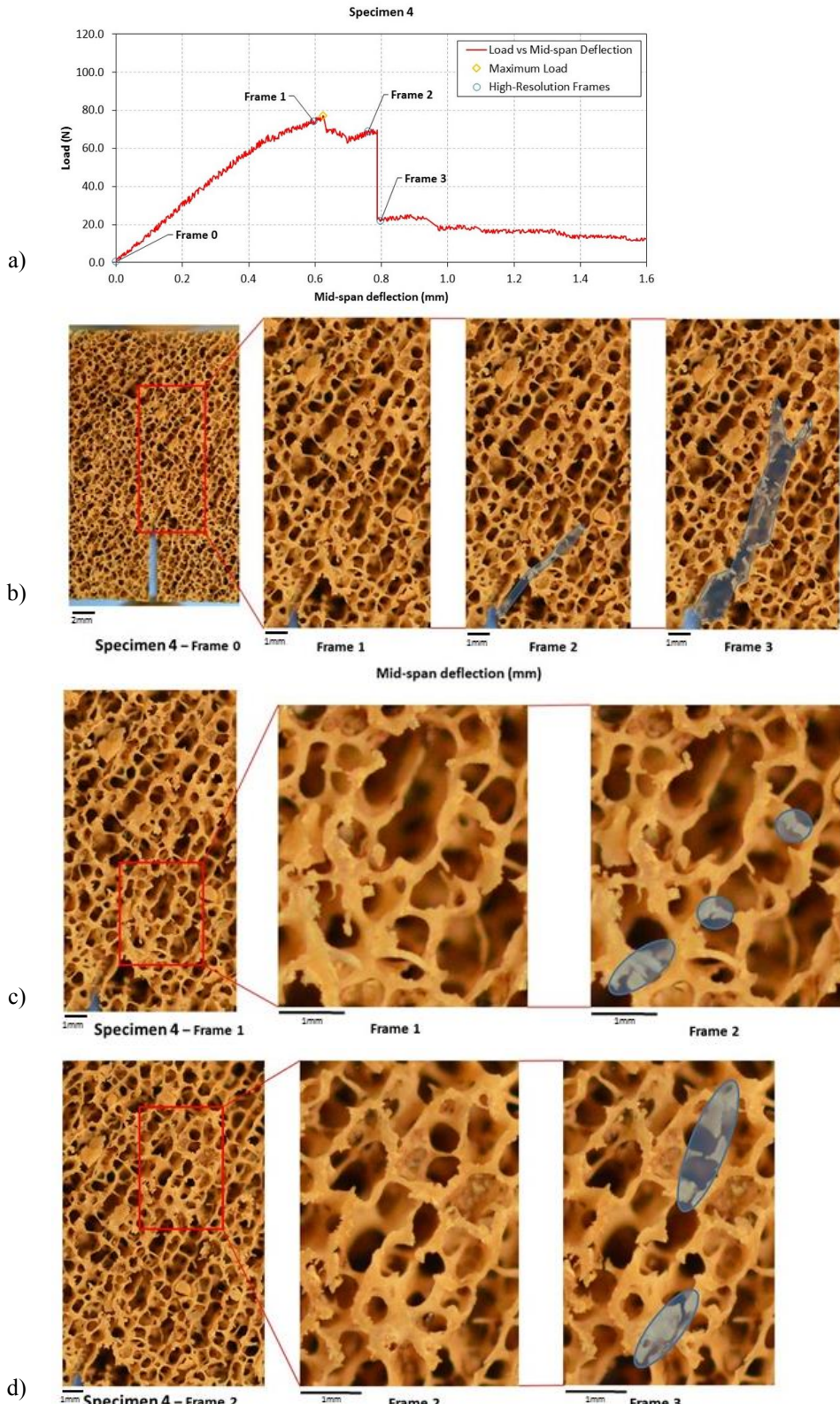


Figure 11 – a) Load –displacement curve for Specimen 4, showing Frames 0 to 4 used in the analysis, b) Frames 0 to 3 showing the staged propagation of a crack from the notch tip, c) close up of Frames 1 and 2 and d) close up of Frames 2 and 3 showing punctual fractures in the trabecula which occur as the main crack that initiated at the notch tip propagates

### 3.5 High-Speed Video camera observations

The HSV camera was used to capture three seconds of video at 5,000 frames per second when a first visible crack of the test was observed. Figures 12a and 12b show the image analysis performed for Specimen 10 using three of the frames captured: one at the start of the test, another at the initiation of the first propagated crack and finally when the crack is arrested i.e. stops propagating. It can be observed that the crack initiated at the tip of the notch and propagated between Frame -2850 and Frame -2846, as the load dropped. Since the crack propagated in four frames and the length of the propagated crack measured from Figure 12b is approximately 8mm, one can estimate that the crack propagated at a speed of  $(0.008\text{m} \cdot 5,000\text{fps})/4\text{frames} = 10\text{m/s}$ . The other tests imaged with the HSV camera show that the duration of crack propagation ranged between two and seven frames which, taking into account the length of the respective propagated cracks, correspond to a speed of crack propagation that varies between 4.0 m/s and 11.0m/s. In this test and in those shown in Appendix 7.3, the cracks appear to propagate in tension, as they open without any visible sliding, as expected for Mode I loading.

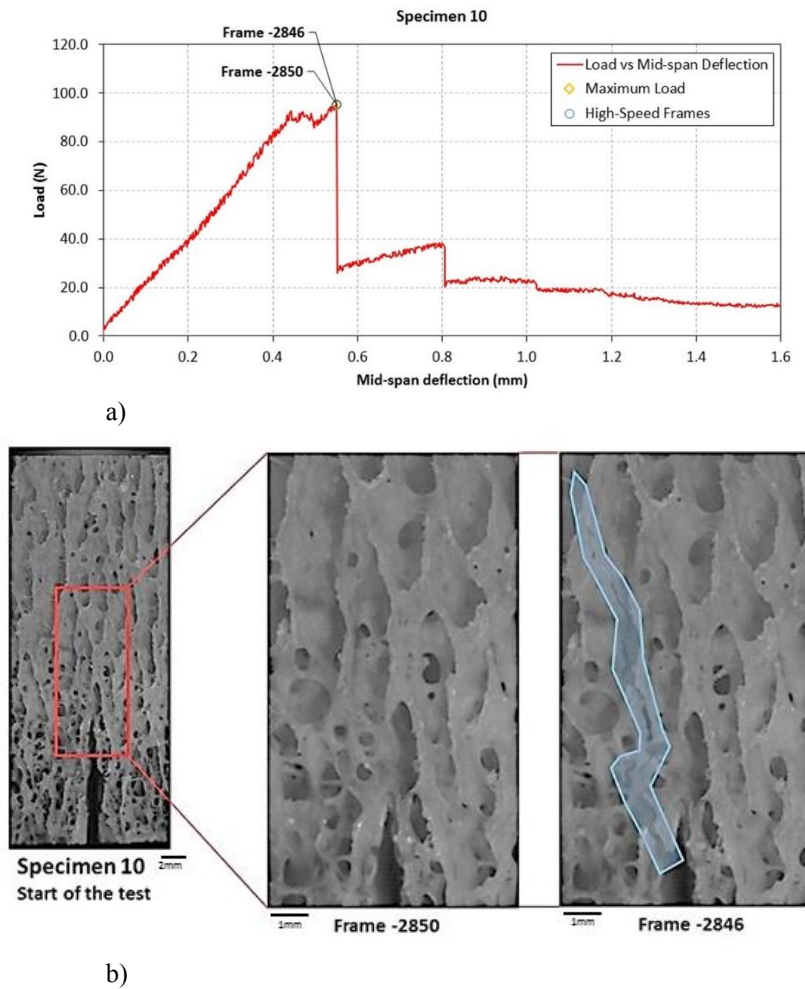


Figure 12 – a) Load –displacement curve for Specimen 10, showing the frames used in the b) HSV image analysis

## 4 Relative density and fracture toughness of the specimens

Several authors, such as Gibson (1985), Rice et al. (1988) and Ford and Keaveny (1996) studied the mechanical behavior of trabecular bone and found that its Elastic Modulus, strength and fracture toughness strongly depend on its relative density, similar to what is observed in other cellular solids. In this Section, the fracture toughnesses and the relative densities of the specimens tested will be analyzed and related to each other.

The fracture toughness for the three-point bending tests performed in this project was calculated based on the ASTM E-1290-08 standard:

$$K_I = \frac{4P_{max}}{B} \sqrt{\frac{\pi}{W}} \left[ 1.6 \left( \frac{a}{W} \right)^{1/2} - 2.6 \left( \frac{a}{W} \right)^{3/2} + 12.3 \left( \frac{a}{W} \right)^{5/2} - 21.2 \left( \frac{a}{W} \right)^{7/2} + 21.8 \left( \frac{a}{W} \right)^{9/2} \right]$$

as well as using Bower equation:

$$K_I = \frac{6P_{max}}{BW} a^{1/2} Y$$

with

$$Y = \frac{1.99 - a/W (1 - a/W) (2.15 - 3.93 a/W + 2.7(a/W)^2)}{(1 + 2 a/W)(1 - a/W)^{3/2}}$$

In these equations,  $P_{max}$  is the maximum vertical load reached in the three-point bending tests, and the letters  $a$ ,  $B$  and  $W$  are defined in Figure 4. As shown in Figures 13a and 13b, the fracture toughness of the specimens varied between  $203 \text{ kN/m}^{3/2}$  and  $395 \text{ kN/m}^{3/2}$  with an average of  $284 \text{ kN/m}^{3/2}$  for Orientation 1 (in the same plane as the radial trabeculae, as defined in Figure 5), and between  $168 \text{ kN/m}^{3/2}$  and  $319 \text{ kN/m}^{3/2}$  with an average of  $225 \text{ kN/m}^{3/2}$  for Orientation 2 (parallel to the axis of the vertebra, as defined in Figure 5). The calculation of the fracture toughnesses is shown in Appendix 7.2 – Relative Density and Fracture Toughness Calculation.

The relative density of the specimens was measured using the methodology explained in Subsection 2.3 – Relative Density Measurement – and their values are shown in Appendix 7.2 for the 12 specimens tested. The relative density of the specimens varies between 21.6% and 26.9% with an average of 24.5% for Orientation 1, and between 19.6% and 22.9% with an average of 21% for Orientation 2. These values are comparable with the relative density of human trabecular bone, which vary between 20% and 25% for a healthy young adult. As shown in Appendix 7.2, the average density of the solid part of the whale

trabecular bone ( $\rho_s$ ) for the 12 specimens was  $2054 \text{ kg/m}^3$ , very similar to the value of  $2060 \text{ kg/m}^3$  reported by Gibson and Ashby (1988) – Table 11.1 – for cow bone.

By looking at Figures 13a and b, one can also notice that the fracture toughness of the bone appears to increase from the outside to the center of the trabecular bone for both cutting directions. In fact, the fracture toughness reaches their maxima near the focal point of the radial trabecula (refer to Figure 5) for both orientations tested.

Furthermore, there appears to be a reasonable correlation between the fracture toughness and the relative density of the specimens, as shown in Figure 14. This is theoretically expected, even though the R2 value obtained was relatively low (0.66). This is very likely due to the fact that the relative density is measured for a 4"-long beam, while the fracture only develops at the mid-span of the specimens. A higher correlation would be expected if smaller specimens are used, so that there is not much material far away from the developing fracture. For this project, using large specimens had the advantage of (1) allowing one to take clear unobstructed pictures with different cameras and (2) being relatively simple to prepare.

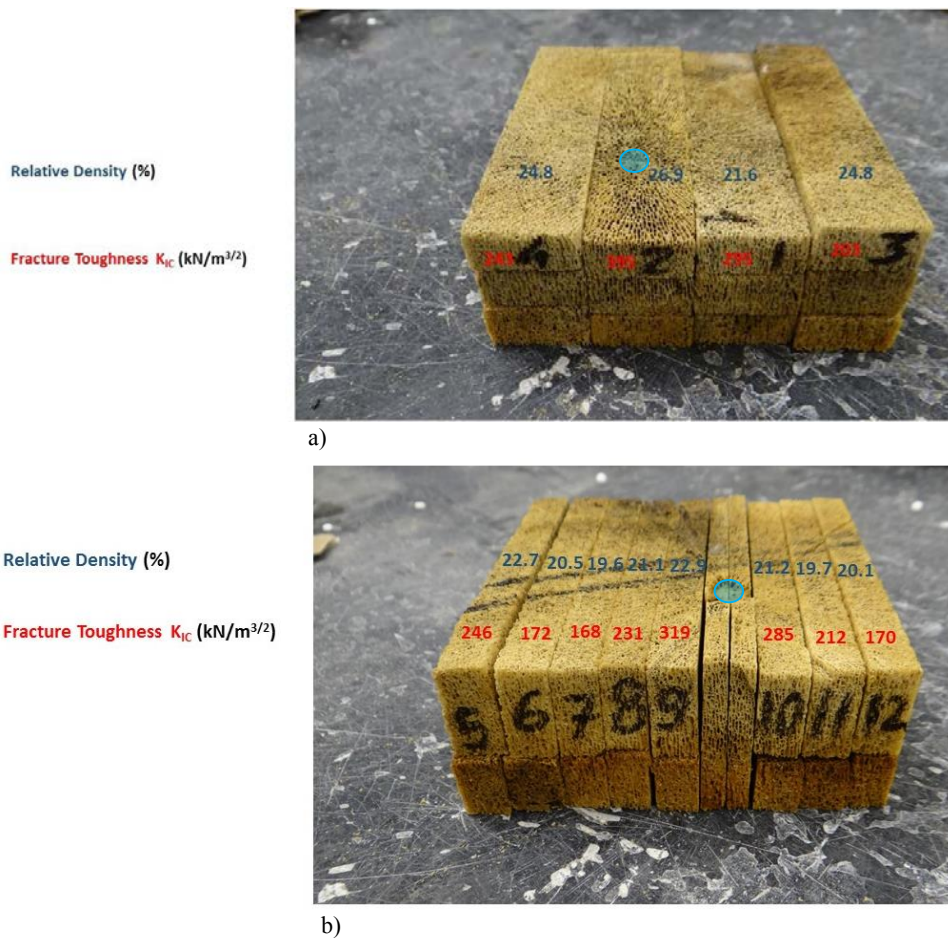


Figure 13 – Relative densities and fracture toughnesses for specimens with a) Orientation 1 and b) Orientation 2. The blue circles represent the focal point of the radial trabeculae, as also defined in Figure 5.

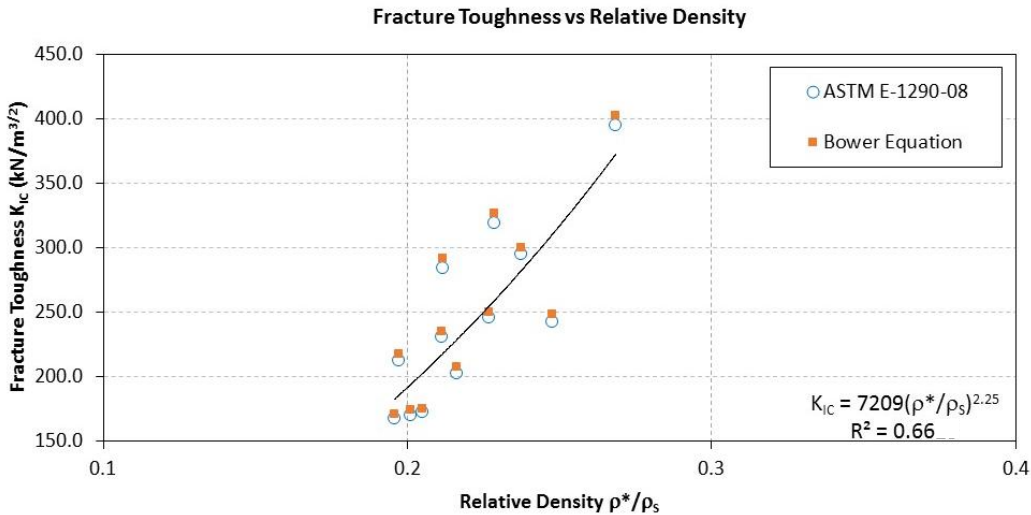


Figure 14 –Relation between relative density and fracture toughness for the specimens tested

## 5 Summary and Conclusions

From the analyses of the results obtained from three-point bending tests performed in 12 specimens of whale trabecular bone it was found that:

- There is a strong correlation between the maximum vertical load reached by the specimens and the slope of the load-displacement curve in the linear elastic regime;
- The fractures initiate at the notch tip and propagate without branching and by stages, causing a load drop every time they propagate;
- For Orientation 1, in which fractures propagate in the same plane as the radial trabeculae, the propagated crack follows the direction of the radial trabeculae.
- The relative densities of the specimens vary from 19.6% to 26.9%. These densities are comparable to human trabecular bone;
- The average absolute density of the solid part of the trabecular bone ( $\rho_s$ ) is 2,054 kg/m<sup>3</sup>, similar to cow bone;
- The average relative densities of the specimens with Orientation 1 (same plane as the radial trabeculae) and Orientation 2 (parallel to the axis of the vertebra) are 24.5% and 21.0%, respectively. Therefore, it appears that the specimens with Orientation 1 are denser than those with Orientation 2;
- The fracture toughnesses are also higher in the specimens with Orientation 1 ( $K_I^{Avg} = 284$  kN/m<sup>3/2</sup>) than with Orientation 2 ( $K_I^{Avg} = 225$  kN/m<sup>3/2</sup>);

- For both specimen orientations, it appears that the fracture toughnesses increase from the outside to the focal point of the radial trabeculae.

In conclusion, this project enhanced the knowledge of the fracturing processes in trabecular bone subject to Mode I loading, not only by relating load-displacement curves with what actually occurs in the specimen via High-Resolution and High-Speed Video images but also by establishing relationships between the maximum vertical load and the slope of the load-displacement curves in the linear elastic regime and between the fracture toughnesses and relative densities of the specimens.

## 6 References

- ASTM 854 – 14 (2014) Standard test methods for specific gravity of soil solids by water Pycnometer. American Society for Testing and Materials, Philadelphia, PA, USA
- ASTM E-1820 (2001) Standard test method for measurement of fracture toughness. American Society for Testing and Materials, Philadelphia, PA, USA
- Bayraktar HH, Morgan EF, Niebur GL, Morris GE, Wong EK, Keaveny TM (2004) Comparison of the elastic and yield properties of human femoral trabecular and cortical bone tissue. *J Biomech* 37:27-35
- Cook RB and Ziopoulos P (2009) The fracture toughness of cancellous bone *J Biomech* 42:2054-2060
- Ford CM and Keaveny TM (1996) The dependence of shear failure properties of trabecular bone on apparent density and trabecular orientation. *J Biomech* 29:1309-1317
- Fyhrie DP and Schaffler MB (1994) Failure mechanisms in human vertebral trabecular bone. *Bone* 15: 105-109
- Gibson LJ (1985) The mechanical behavior of cancellous bone. *J Biomech* 18(5):317-328
- Gibson LJ and Ashby MF (1988) Cellular Solids: Structure and Properties. First Ed. Pergamon Press, New York, USA
- Hardisty MR, Garcia TC, Choy S, Dahmubed J, Stover SM, Fyhrie DP (2013) Stress-whitening occurs in demineralized bone. *Bone* 57:367-374
- Keavenly TM, Guo E, Wachtel EF, McMahon TA, Hayes WC (1994) Trabecular bone exhibits linear elastic behavior and yields at low strains. *J Biomech* 27(9):1127-1136
- Keavenly TM, Wachtel EF, Kopperdahl DL (1999) Mechanical behavior of human trabecular bone after overloading. *J Orthop Res* 17:346-353

Muller R, Gerber SC, Hayes WC (1998) Micro-compression: a novel technique for the nondestructive assessment of local bone failure. *Technology and Health Care* 6:433-444

Nagaraja S, Couse TL, Guldberg RE (2005) Trabecular bone microdamage and microstructural stresses under uniaxial compression *J Biomech* 38:707-716

Rice JC, Cowin SC, Bowman JA (1988) On the dependence of the elasticity and strength of cancellous bone on apparent density *J Biomech* 21(2):155-716

Thurner PJ, Erickson B, Jungmann R, Schriock Z, Weaver JC, Fantner GE, Schitter G, Morse DE, Hansma PK (2009) High-Speed photography of compressed human trabecular bone correlates whitening to microscopic damage. *Eng Fract Mech* 74:1928-1941

## 7 Appendices

### 7.1 Specimens and Cracks Dimensions

Specimen	Mass (g)	Thickness (mm)						Width (mm)					Height (mm)					
		1	2	3	4	5	6	Average	1	2	3	4	Average	1	2	3	4	Average
1	15.959	12.53	12.64	12.22	12.21	12.05	12.44	12.35	25.65	25.52	25.13	25.09	25.35	103.65	103.12	103.77	102.83	103.34
2	17.331	12.47	12.53	12.18	11.18	11.92	12.33	12.10	25.17	24.98	24.6	24.36	24.78	103.86	103.26	103.93	103.22	103.57
3	15.819	14.03	14.16	14.12	14.01	13.72	13.77	13.97	25.7	25.39	24.95	24.84	25.22	101.76	102.48	103.23	101.78	102.31
4	16.897	11.8	11.5	11.47	11.57	11.66	11.92	11.65	25.6	25.9	26.25	26.36	26.03	104.46	104.38	104.06	104.34	104.31
5	16.375	13.37	12.14	12.62	12.7	13.44	13.1	12.90	25.25	25.29	25.82	26.1	25.62	107.73	107.23	107.22	107.95	107.53
6	14.251	11.82	12.4	12.73	12.75	12.81	11.88	12.40	25.87	26.15	25.76	25.64	25.86	108.06	106.92	107.24	107.88	107.53
7	12.601	11.09	11.35	11.46	11.78	11.79	10.92	11.40	25.66	25.77	25.78	25.64	25.71	107.11	107.34	107.87	107.05	107.34
8	12.817	10.76	10.98	11.28	11.46	11.47	10.57	11.09	24.65	25.13	25.32	25.49	25.15	106.82	106.77	106.83	106.76	106.80
9	14.843	11.5	11.76	11.91	11.98	11.42	10.87	11.57	25.64	25.65	26.15	25.99	25.86	106.71	106.91	107	106.66	106.82
10	13.902	11.48	11.6	11.58	11.67	11.5	11.54	11.56	25.23	25.17	25.4	25.64	25.36	109.1	108.77	108.94	108.76	108.89
11	12.969	11.72	11.42	11.22	11.19	11.05	11.55	11.36	26.15	26.32	25.92	25.76	26.04	108.98	109.13	108.97	108.82	108.98
12	12.823	11.62	11.46	11.27	11.2	10.95	10.97	11.25	25.32	25.49	25.76	25.93	25.63	108.51	108.78	108.69	108.41	108.60

Specimen	a		a average
	(mm)		
1	12.6	12.95	12.86
2	12.15	12.07	12.3
3	7.13	6.96	7
4	7.63	7.82	7.77
5	12.52	12.54	12.69
6	12.81	12.85	12.69
7	12.83	13.03	13.03
8	12.42	12.28	12.3
9	6.98	7.31	6.97
10	6.56	7.08	6.92
11	6.96	7.08	6.95
12	7.23	7.22	7.16

## 7.2 Relative Density and Fracture Toughness Calculations

### Relative Density Calculation

Specimen	Weight of Specimen $W_s$	Weight of Pycnometer ( $W_p$ )	Weight of pycnometer + water ( $W_{pw}$ )	Weight of pycnometer + water + specimen ( $W_{ps}$ )	Water Temperature (T)	Density of water	$G_s$	Density of solid part of bone
	(g)	(g)	(g)	(g)	(°C)	(g/cm³)		(kg/m³)
1	15.959	348.33	633.92	642.21	20.3	0.9981440	2.077	2077
2	17.331	348.33	633.92	642.93	23.4	0.9974456	2.077	2077
3	15.819	348.33	633.92	641.96	18.0	0.9985976	2.031	2031
4	16.897	348.33	633.92	643.00	20.3	0.9981440	2.158	2158
5	16.375	348.33	633.92	642.26	22.8	0.9975412	2.033	2033
6	14.251	348.33	633.92	641.12	20.7	0.9980594	2.017	2017
7	12.601	348.33	633.92	640.37	19.9	0.9982269	2.045	2045
8	12.817	348.33	633.92	640.46	19.8	0.9982474	2.038	2038
9	14.843	348.33	633.92	641.47	21.0	0.9979948	2.031	2031
10	13.902	348.33	633.92	641.08	19.9	0.9982269	2.058	2058
11	12.969	348.33	633.92	640.55	20.5	0.9981019	2.042	2042
12	12.823	348.33	633.92	640.46	20.9	0.9980164	2.037	2037

Average	2.054	2054
Std Deviation	0.036	36

Average - Orient1	2.086	2086
Std Deviation - Orient1	0.046	46

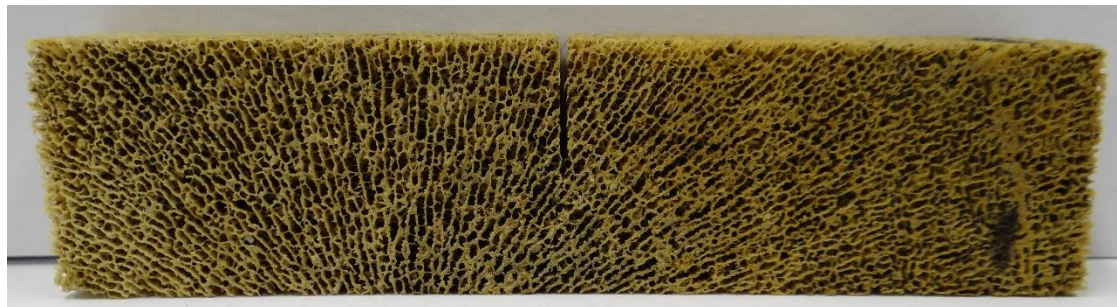
Average - Orient2	2.038	2038
Std Deviation - Orient2	0.011	11

### Fracture Toughness Calculation

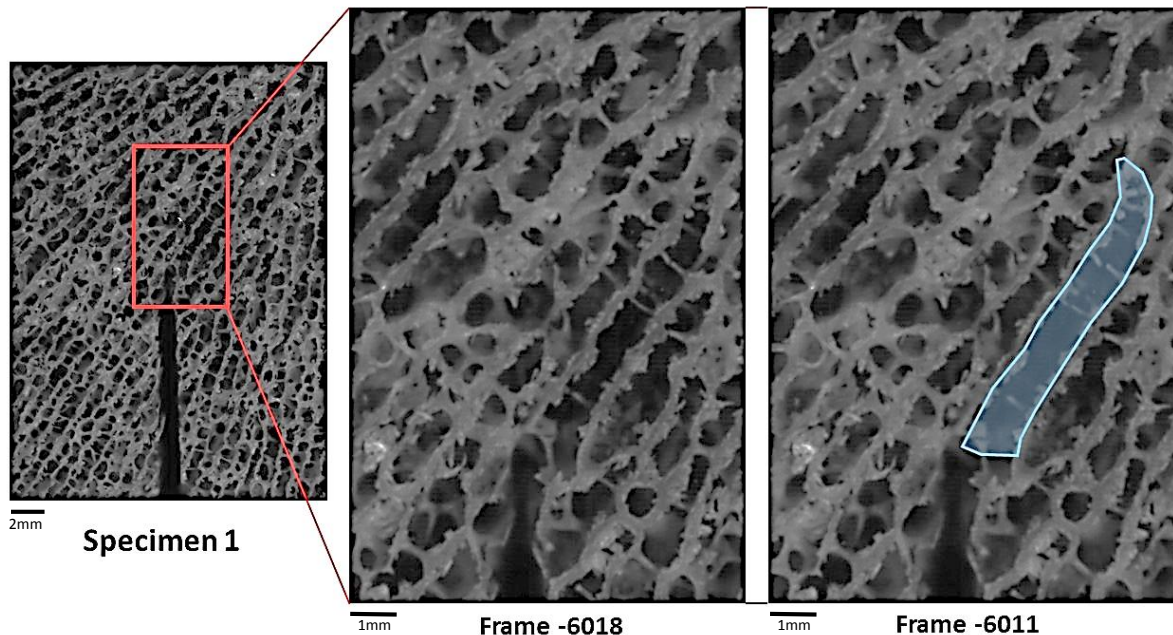
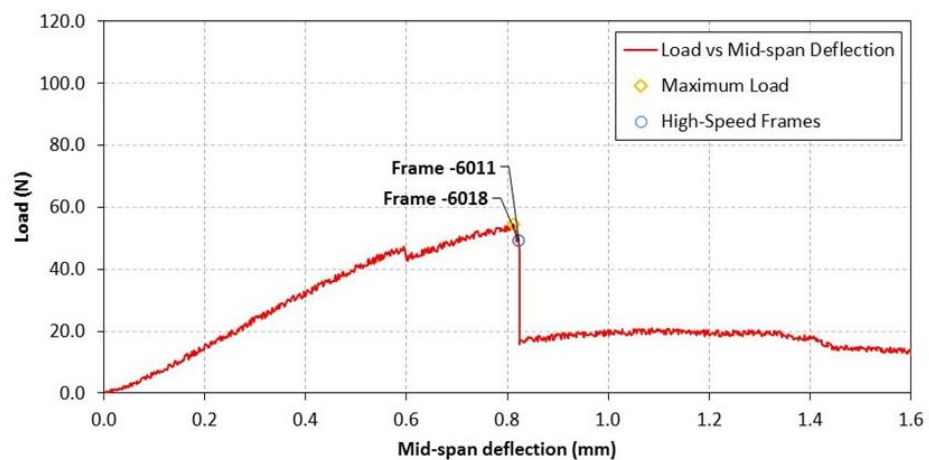
Specimen	Relative Density	a (m)	W (m)	B (m)	P (N)	Y (ASTM)	Y (Bower)	KI (ASTM) kN/m <sup>3/2</sup>	KI (Bower) kN/m <sup>3/2</sup>	KIAvg (ASTM)
1	0.238	0.01280	0.02535	0.01235	54.44	1.50	2.54	294.67	299.75	284
2	0.269	0.01217	0.02478	0.01210	73.93	1.44	2.46	394.92	402.16	
3	0.216	0.00703	0.02522	0.01397	79.87	0.79	1.82	202.61	207.52	
4	0.248	0.00774	0.02603	0.01165	77.20	0.83	1.85	242.52	248.21	
5	0.227	0.01258	0.02562	0.01290	49.87	1.43	2.46	245.83	250.34	
6	0.205	0.01278	0.02586	0.01240	33.41	1.45	2.48	172.27	175.39	
7	0.196	0.01296	0.02571	0.01140	28.91	1.50	2.53	167.81	170.72	
8	0.211	0.01233	0.02515	0.01109	40.02	1.43	2.46	230.98	235.23	
9	0.229	0.00709	0.02586	0.01157	106.76	0.78	1.81	318.95	326.74	
10	0.212	0.00685	0.02536	0.01156	95.17	0.78	1.81	284.52	291.53	
11	0.197	0.00700	0.02604	0.01136	71.01	0.77	1.81	212.43	217.69	
12	0.201	0.00720	0.02563	0.01125	54.15	0.80	1.82	170.32	174.42	

### 7.3 Image Analyses

#### Specimen 1



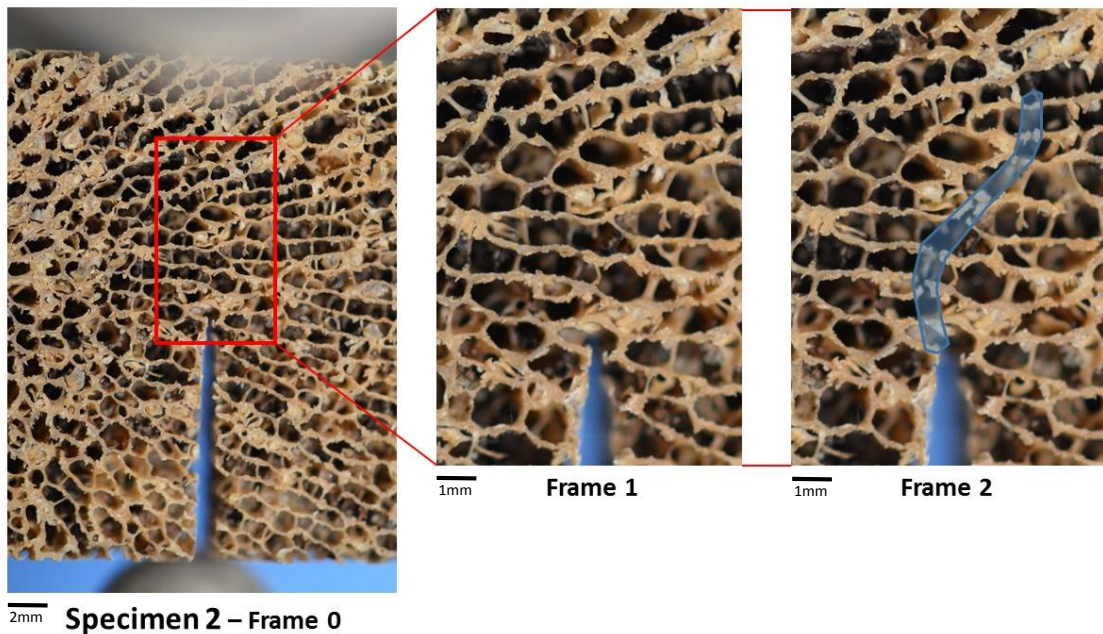
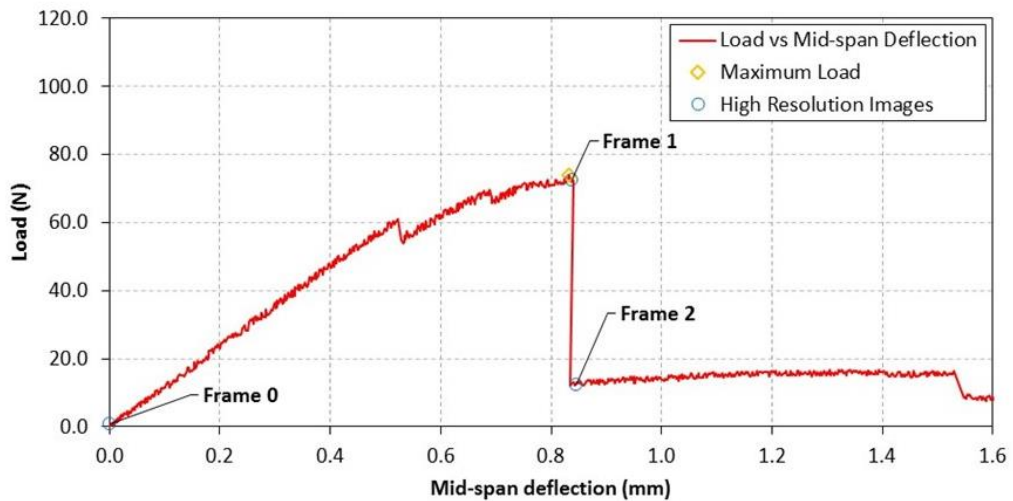
Specimen 1



## Specimen 2



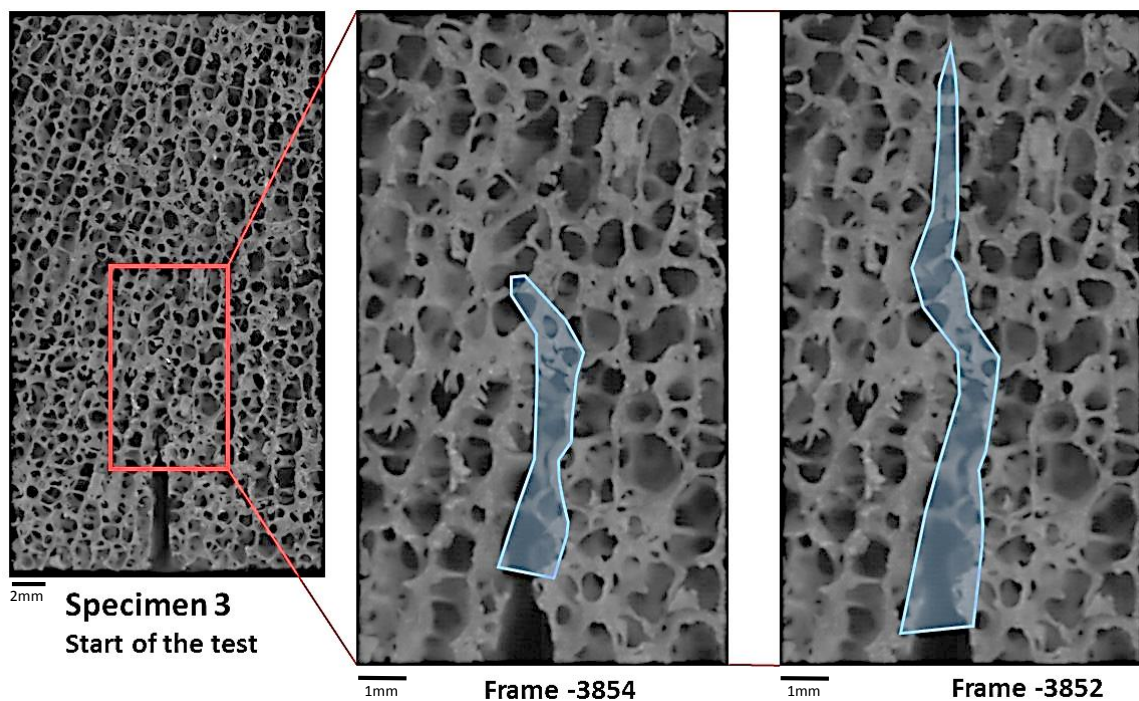
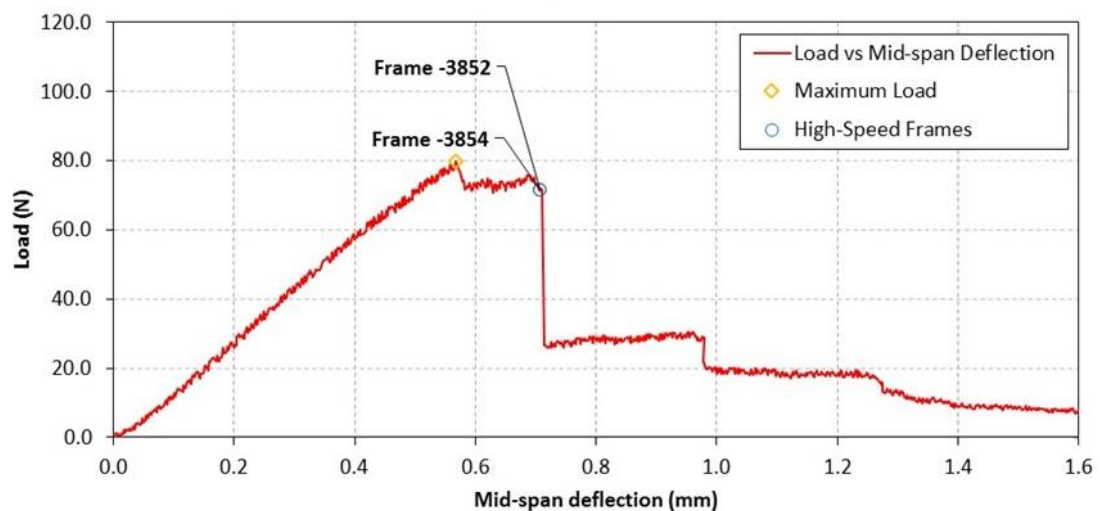
Specimen 2



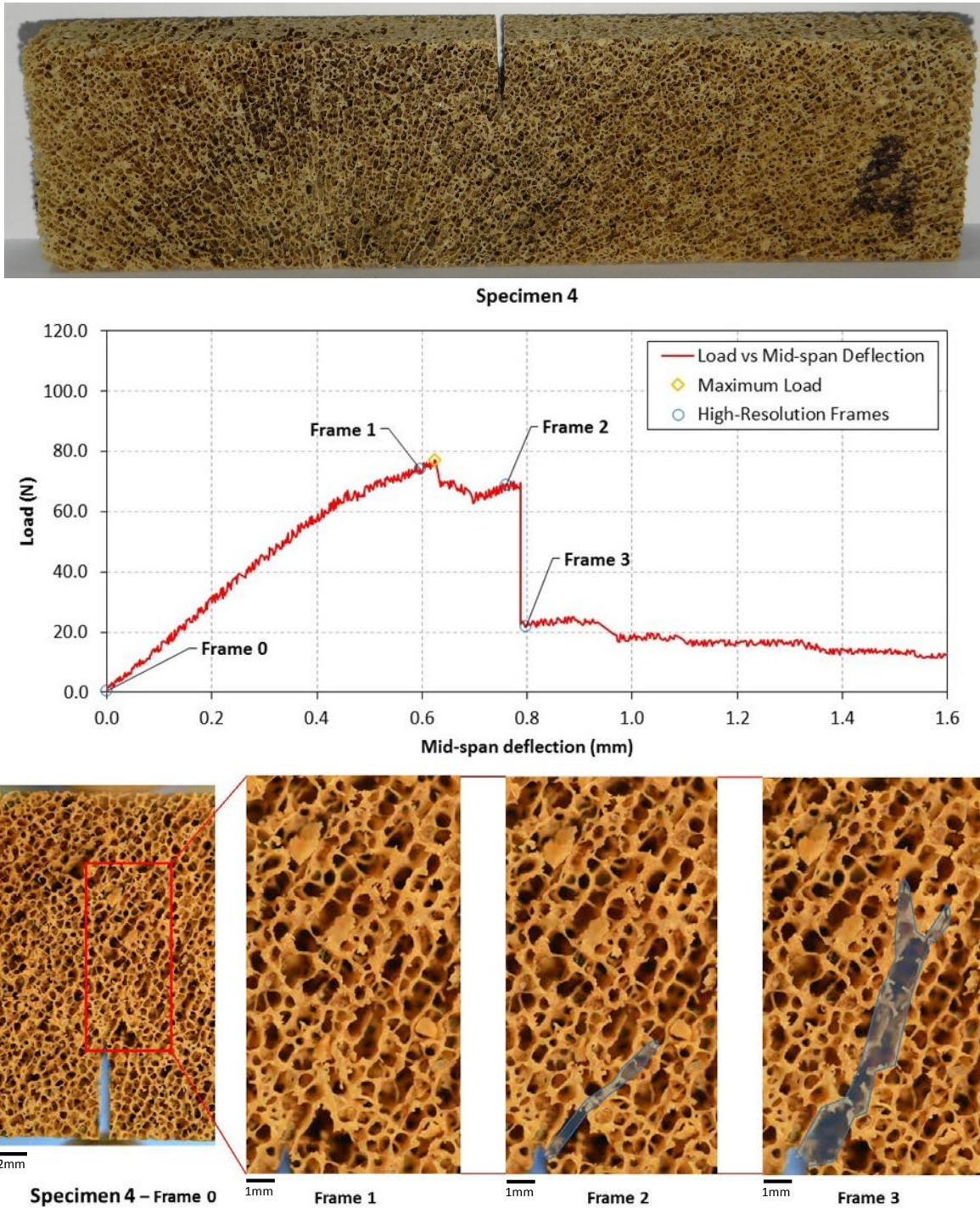
### Specimen 3

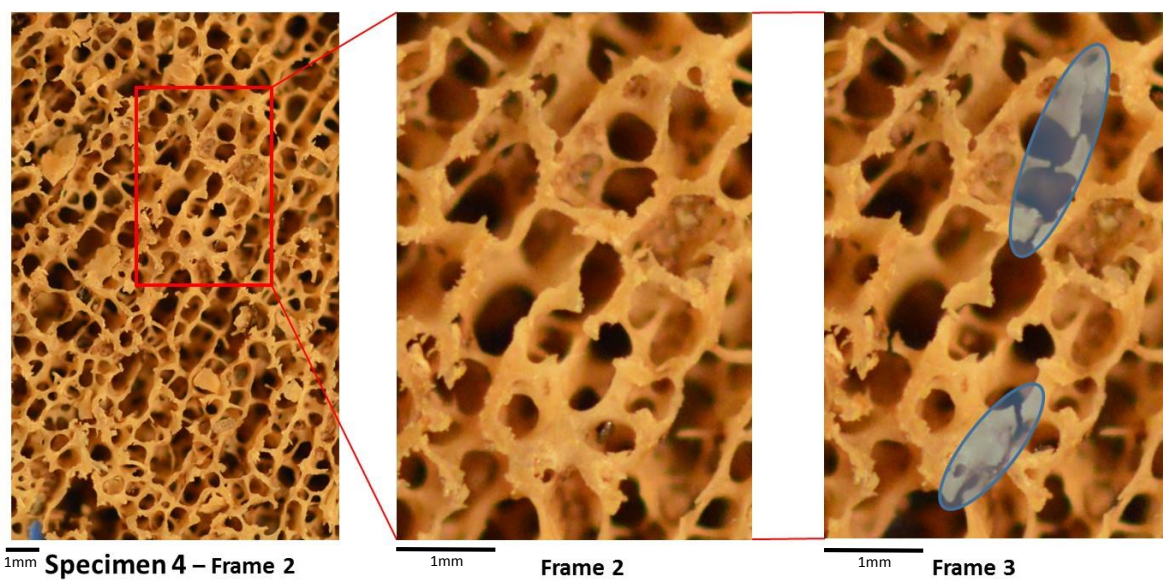
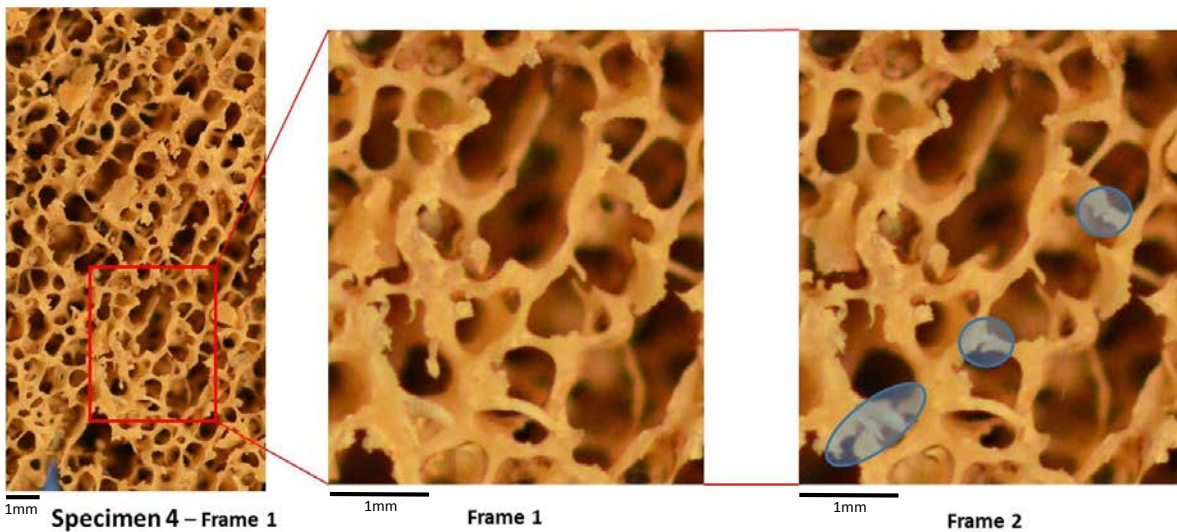


Specimen 3



### Specimen 4

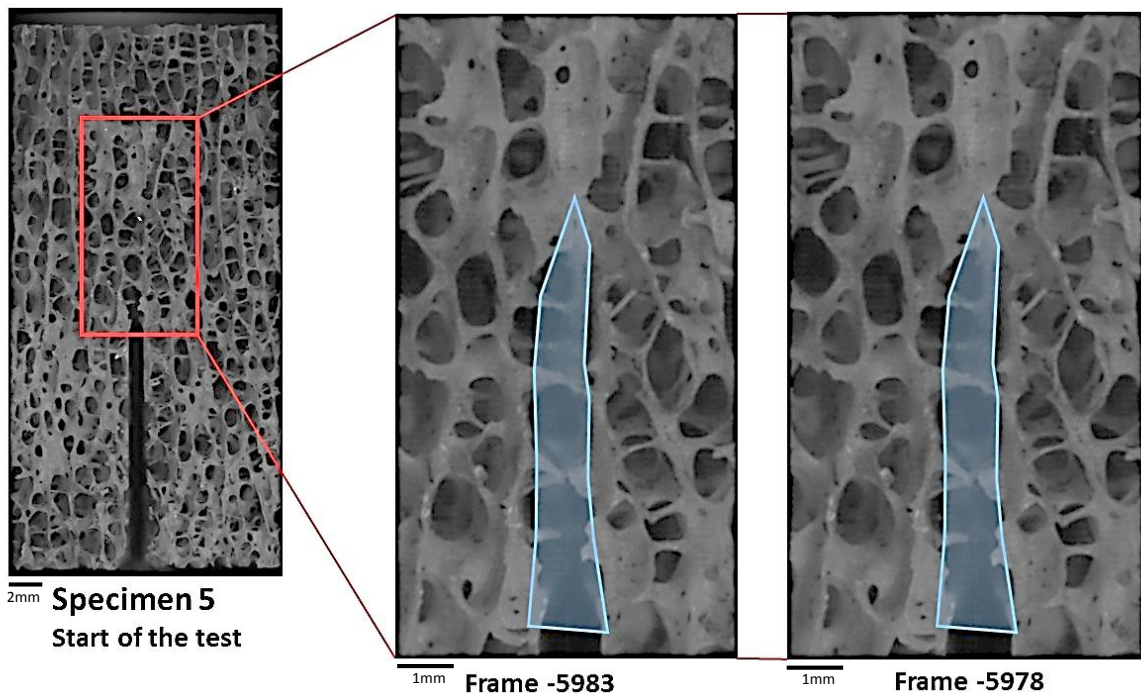
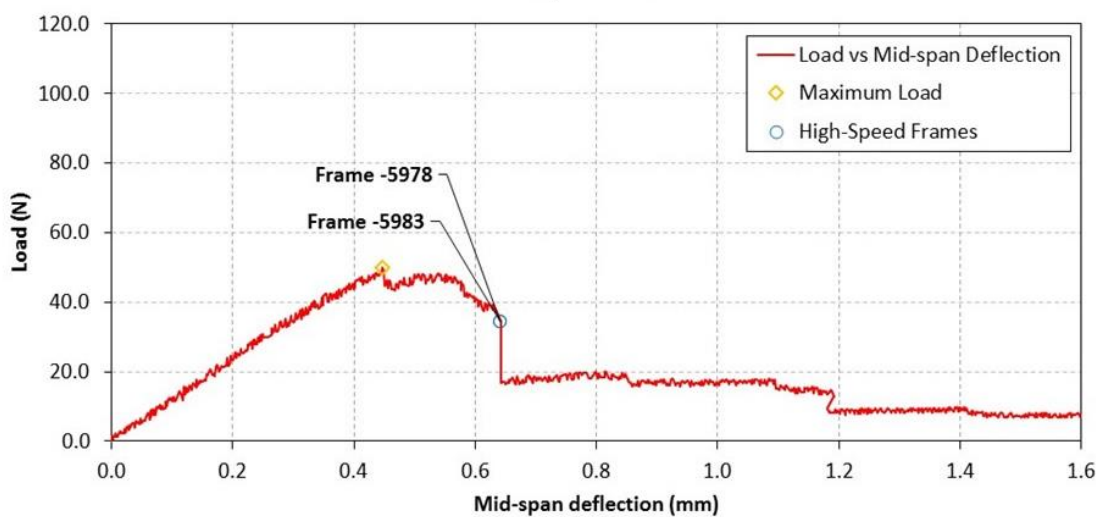




### Specimen 5



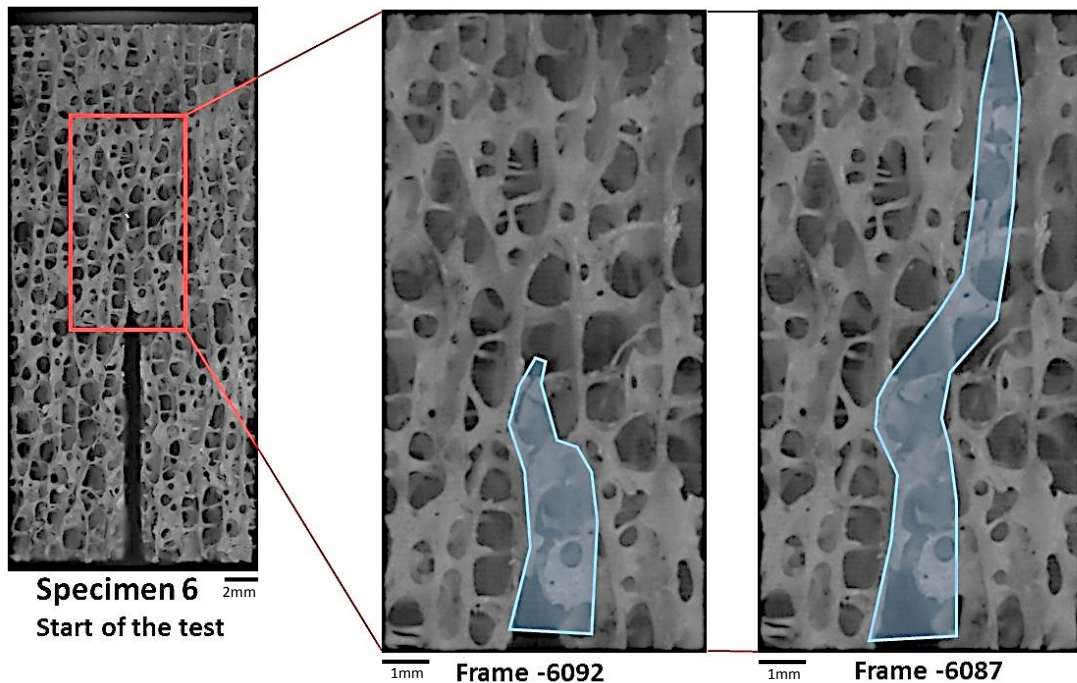
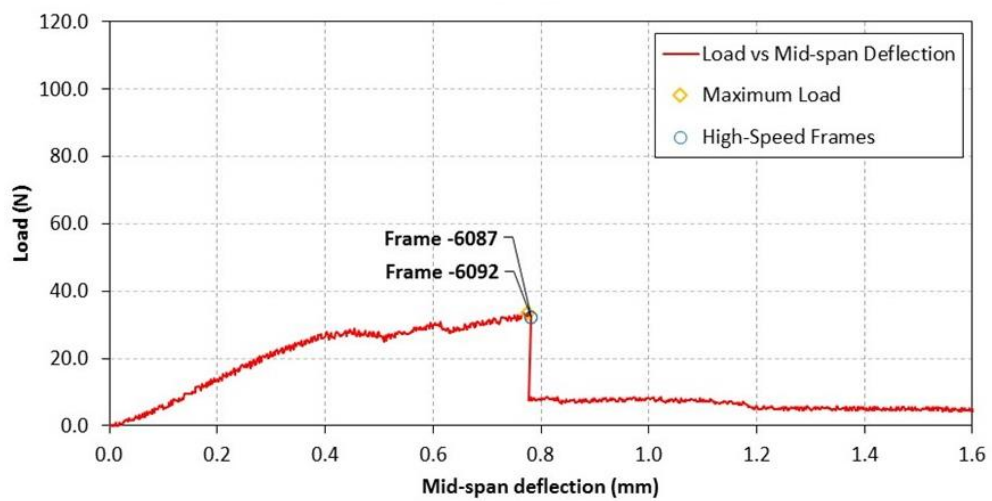
Specimen 5



### Specimen 6



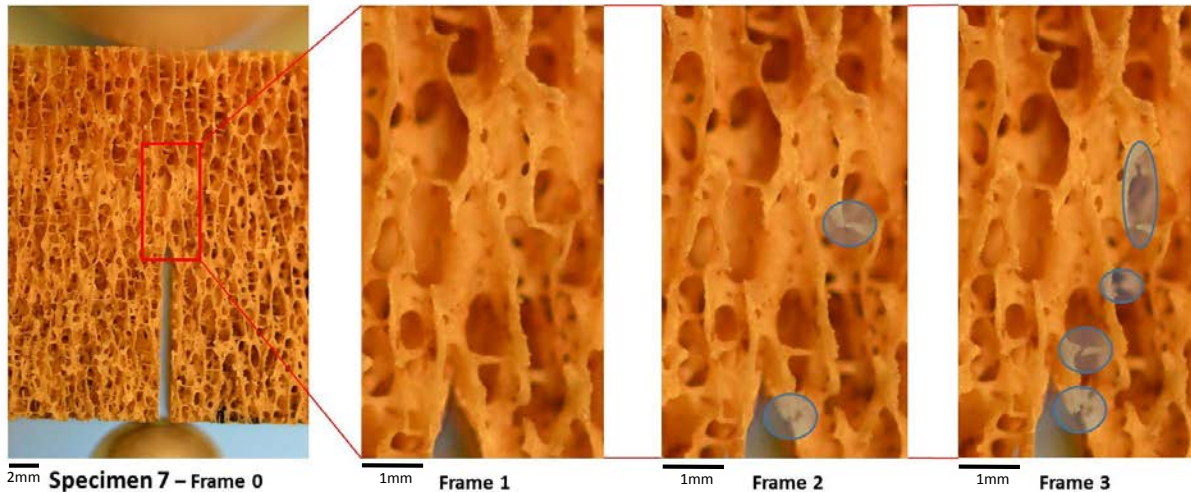
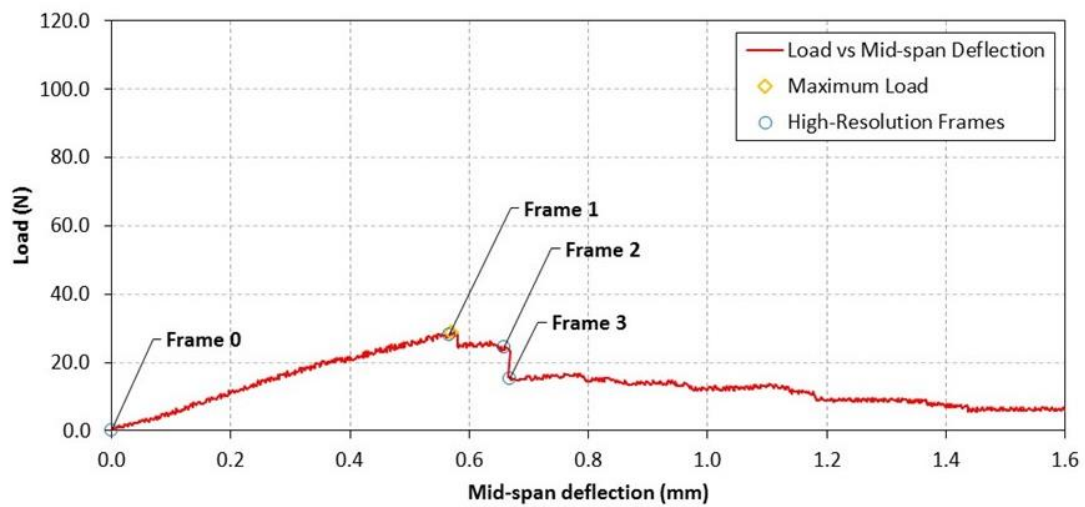
Specimen 6



### Specimen 7



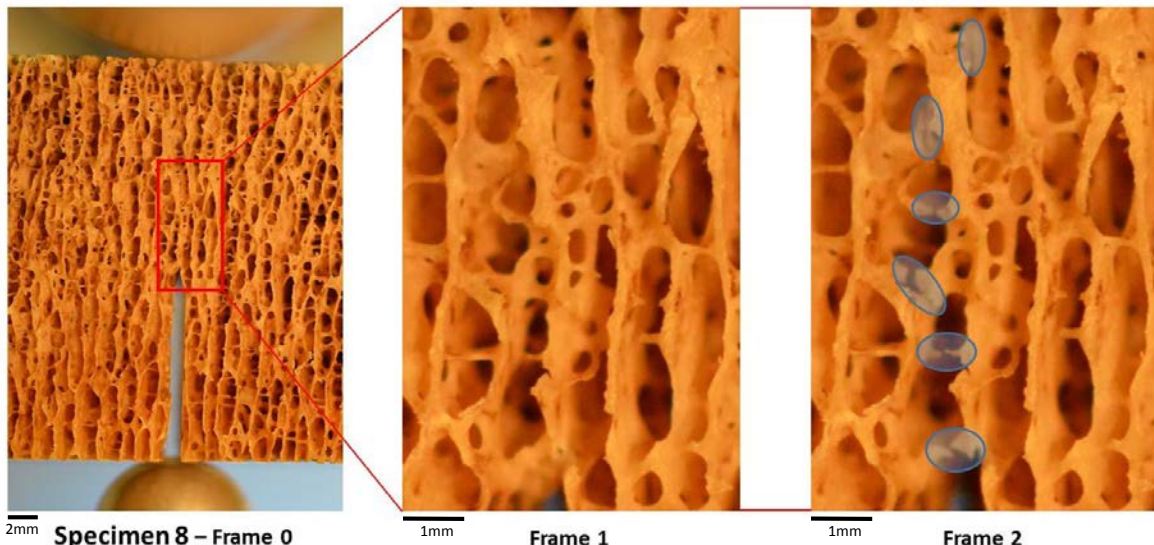
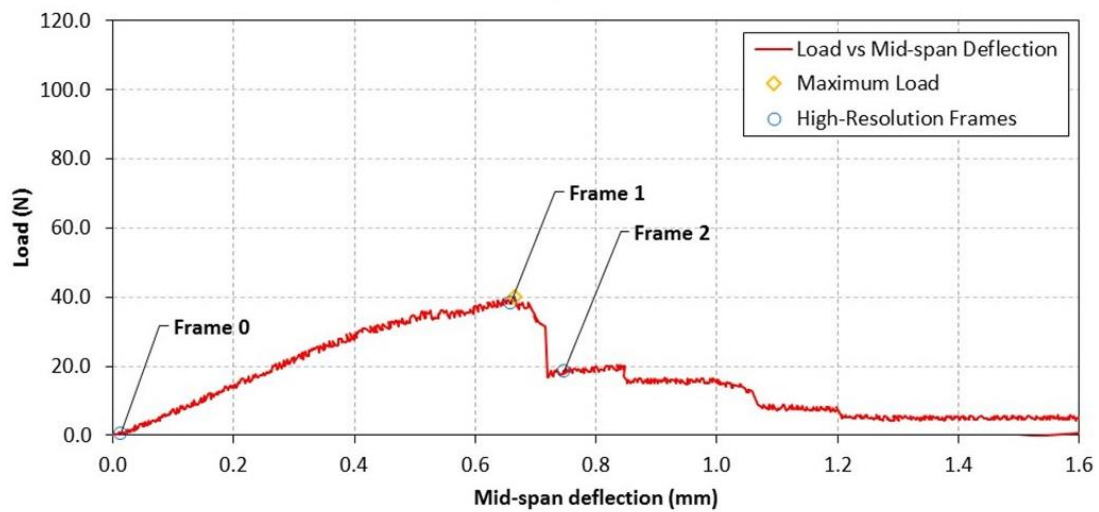
Specimen 7



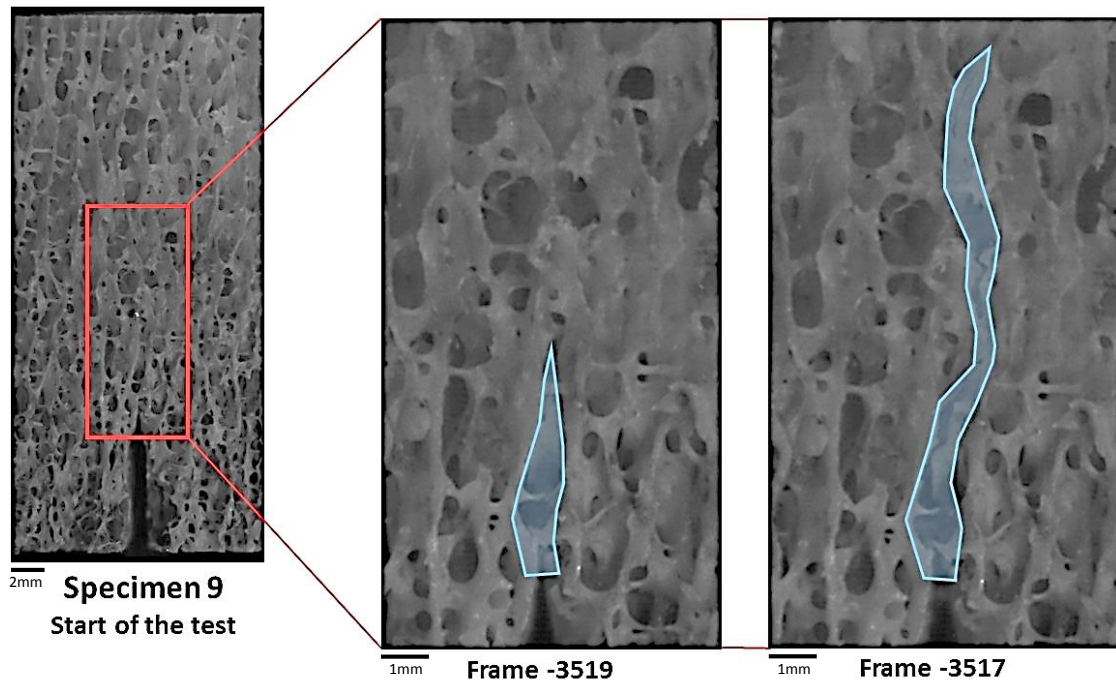
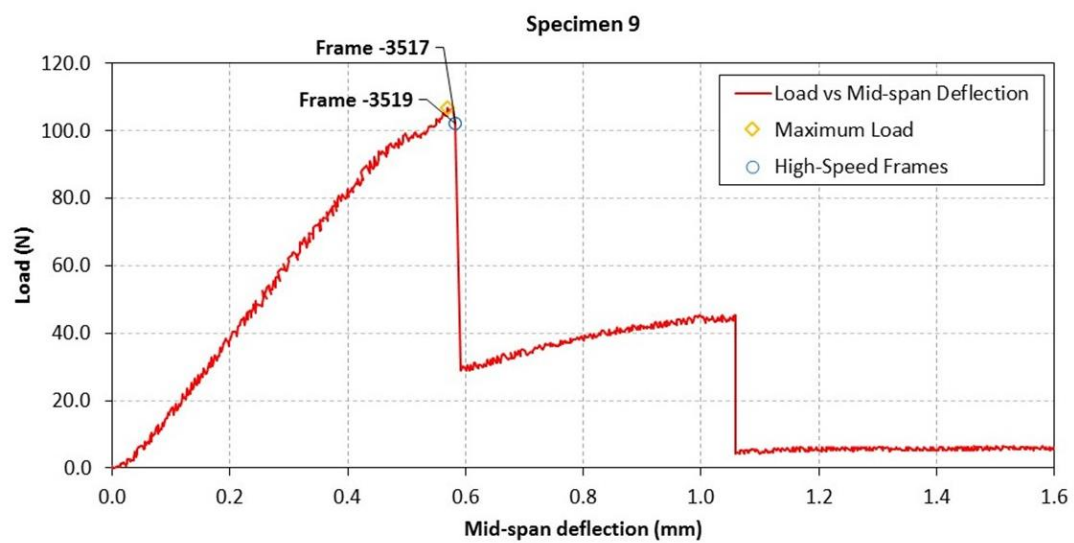
### Specimen 8



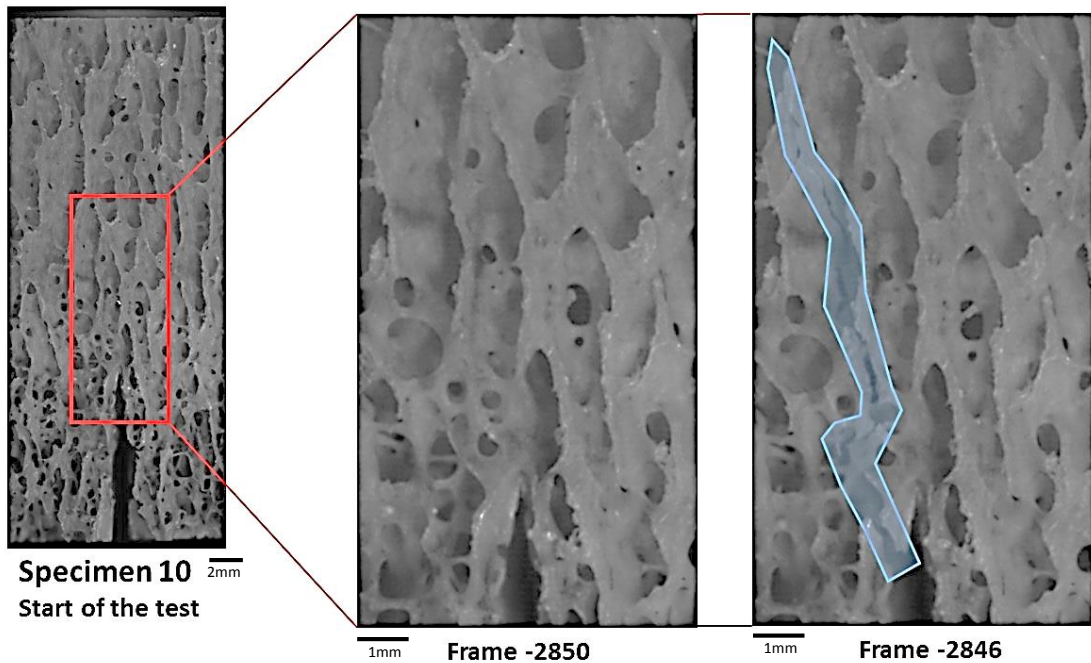
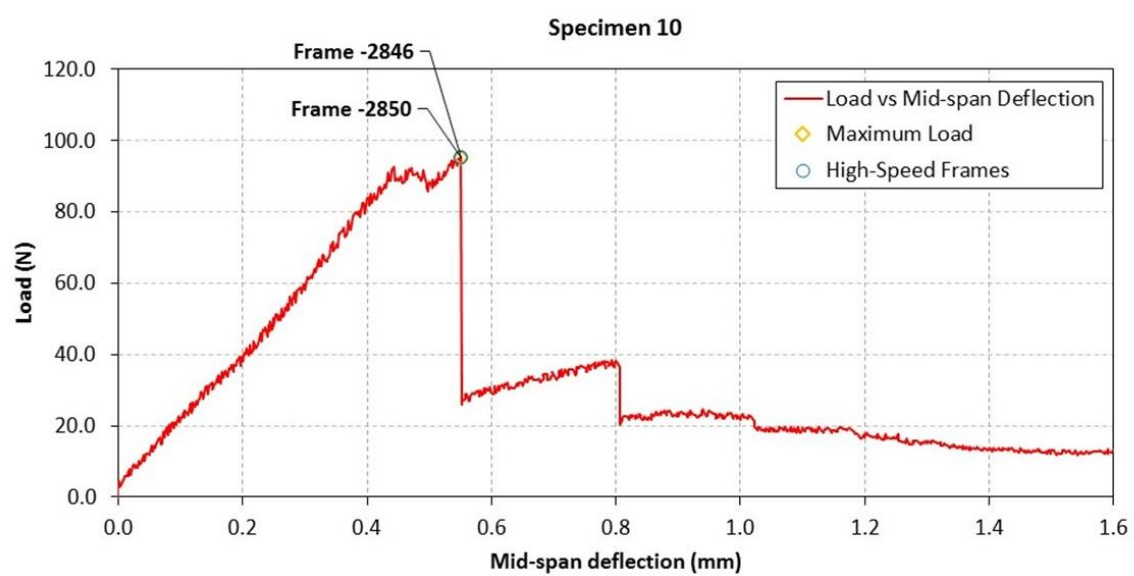
Specimen 8



### Specimen 9



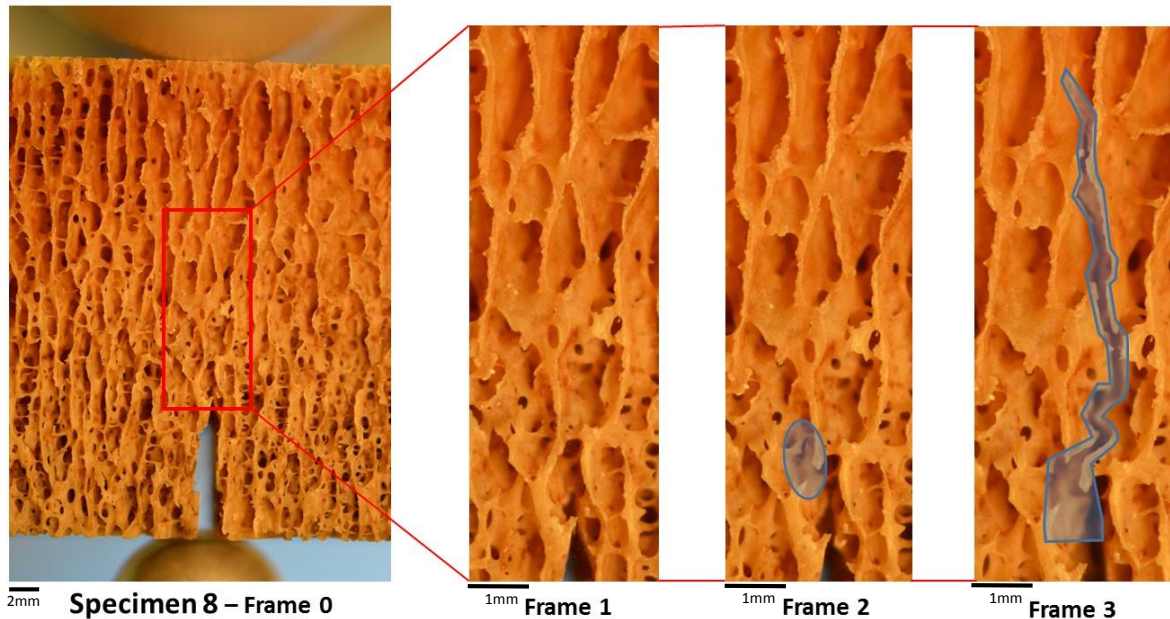
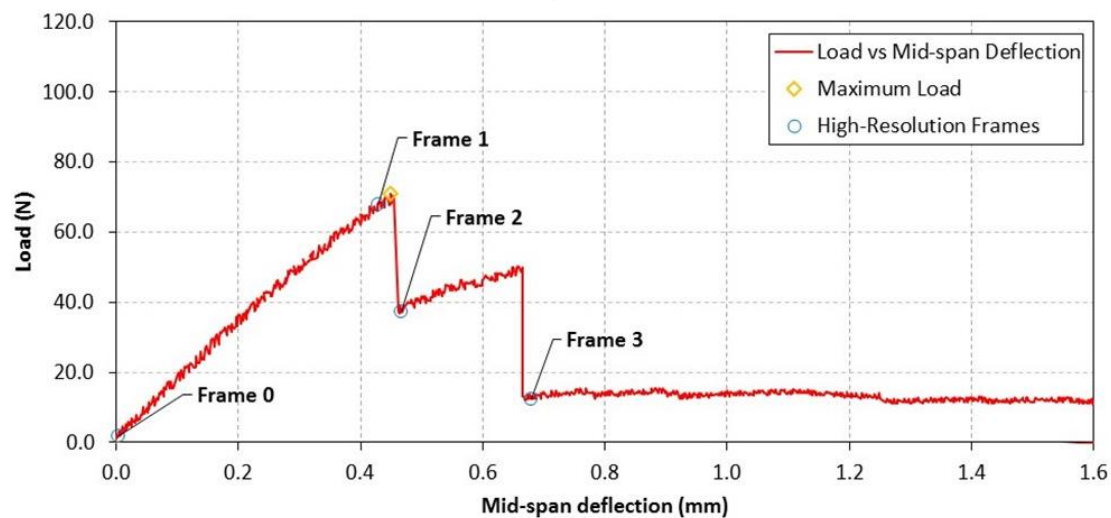
### Specimen 10



### Specimen 11



Specimen 11



Specimen 8 – Frame 0

1mm Frame 1

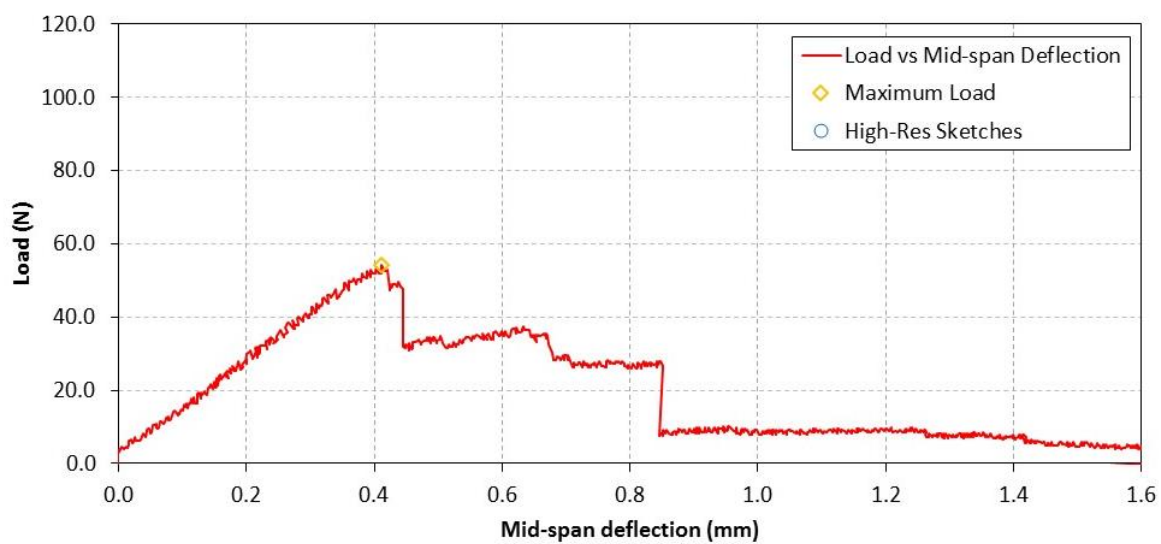
1mm Frame 2

1mm Frame 3

### Specimen 12



**Specimen 12**



(No High-Resolution Frames were collected in this test)

MIT OpenCourseWare  
<http://ocw.mit.edu>

3.054 / 3.36 Cellular Solids: Structure, Properties and Applications  
Spring 2015

For information about citing these materials or our Terms of Use, visit: <http://ocw.mit.edu/terms>.